DEVELOPMENT AND COMMISSIONING OF A VARIABLE CAPACITY EXPERIMENTAL INFRASTRUCTURE FOR A NOVEL THREE FLUID HEAT EXCHANGER

By

Farhan Istiaque

Bachelor of Science in Mechanical Engineering.
Bangladesh University of Engineering and Technology
Dhaka, Bangladesh
2017

Submitted to the Faculty of the
Graduate College of
Oklahoma State University
in partial fulfillment of
the requirements for
the Degree of
Master of Science
May, 2023

DEVELOPMENT AND COMMISSIONING OF A VARIABLE CAPACITY EXPERIMENTAL INFRASTRUCTURE FOR A NOVEL THREE FLUID HEAT EXCHANGER

Thesis Approved:

Dr. Christian K. Bach

Thesis Advisor

Dr. Jeffrey D. Spitler

Dr. Craig R. Bradshaw

ACKNOWLEDGMENTS

One of the most challenging decisions of my life was to come to the USA and start my MS journey. I wouldn't have been able to take this bold step without continuous encouragement from my wife and my parents. My wife supported me at every step of my journey here and my parents supported me financially and mentally whenever I needed them most.

I was lucky to have Dr. Bach as my supervisor and mentor here at OSU during my M.S. He always guided me and pushed me to take on new challenges. I will always be grateful to him for giving me this amazing opportunity to work at his lab.

I would like to thank all my friends and colleagues from the BETSRG group who always helped me and gave me advice.

I am really grateful to have some amazing UGRAs like Jacob Taylor, Emma Laureen Cooley, Cody Schlather, and Joshua Hall. Without them, building a test setup for TriCoil™ in such a short time was impossible. Mr. Aaron Bell also helped us with brazing and gave us valuable advice during the construction of the test setup.

I would also like to thank Johnson Controls for their donation of the indoor and outdoor unit and the fabrication of 1st generation of TriCoil™.

Acknowledgments reflect the views of the author and are not endorsed by committee members or Oklahoma State University.

Name: Farhan Istiaque

Date of Degree: May, 2023

Title of Study: DEVELOPMENT AND COMMISSIONING OF A VARIABLE CAPACITY EXPERIMENTAL INFRASTRUCTURE FOR A NOVEL THREE FLUID HEAT EXCHANGER

Major Field: Mechanical and Aerospace Engineering

Abstract: One of the major problems with using renewable energy is the mismatch between power generation and demand as renewable energy generation and energy usage from HVAC equipment depend on unsynchronized natural factors. To reduce this supply-demand mismatch many researchers suggested using thermal energy storage to shift cooling and/or heating loads. A thermal energy storage (TES) tank can be integrated with building heating and cooling systems using several methods described in the open literature. This thesis explores a novel method to integrate water-based TES with an indoor air coil using a three fluid heat exchanger (TriCoil™). The three fluid heat exchanger will thermally connect water from the TES, refrigerant from the outdoor unit, and indoor air. A test setup has been developed inside the Psychrometric Coil Testing Facility of Oklahoma State University (OSU) to test the TriCoil™. The heat balance of the test setup for different operation modes and test points was within ±5%. An uncertainty analysis has been performed on the test results and major sources of uncertainties have been identified. In the experiment done for this thesis, water from the TES was successfully charged up to 15 kW (cooling) with a log mean temperature difference (LMTD) of 18.5 K using a 4-ton capacity outdoor unit. TriCoil™ was also used to discharge the water from TES with a max capacity of 11.5 kW (heating) with an LMTD of 8.7 K, a water flow rate of 1700 kg/h, and an airflow rate of 1600 CFM.

TABLE OF CONTENTS

Chapter Page

LIST OF TABLES

Table Page

LIST OF FIGURES

Figure Page

Figure Page

CHAPTER I

INTRODUCTION

1.1 Background

Heating, Ventilation, and Air Conditioning (HVAC) is one of the major sources of energy consumption around the world. According to EIA (2022) commercial buildings consume 25% of total energy in the whole U.S.A in 2018. Of this consumption, 32% is for space heating, 9% is for cooling, 11% is for ventilation, and 5% is for refrigeration [EIA (2018)]. The residential sector consume around 29% of total electricity consumption [EIA (2022)] in 2018 and 43% was for space heating, 19% was for water heating, 8% was for air conditioning and 3% was for refrigeration. It becomes obvious how much emphasis should be put into making HVAC components more efficient. This amount of energy consumption has a huge negative impact on our environment. If we can utilize renewable energy in the HVAC sector to reduce the usage of natural fuels and electricity, it would be beneficial for us.

One of the major problems with renewable power generation is the transient nature of power demand and generation [Liu et al. (2019)]. From Figure 1.1, when the demand is at peak at 04:00 PM the generation is lowest. Also, around 04:00 AM, the generation is highest, but the demand is lowest. Many researchers worldwide suggest using Thermal Energy Storage (TES) for demand side management [Arteconi et al. (2012); Cirocco et al. (2022); Saffari et al. (2018)]. If the excess energy during 04:00 AM (Figure 1.1) can be stored in a thermal energy storage system (TES), it can later be used at 04:00 PM when the demand is highest. Sultan et al. (2021) found that peak energy demand can be reduced by 87.5% by using TES. This thesis investigated a

novel approach for integrating the TES into the residential heating and cooling system by using a novel three-fluid heat exchanger. This will allow us to use thermally stored renewable energy for residential heating and cooling even when the energy demand is high with renewable energy supply being low and potentially cutting out a major portion of energy expenditure.

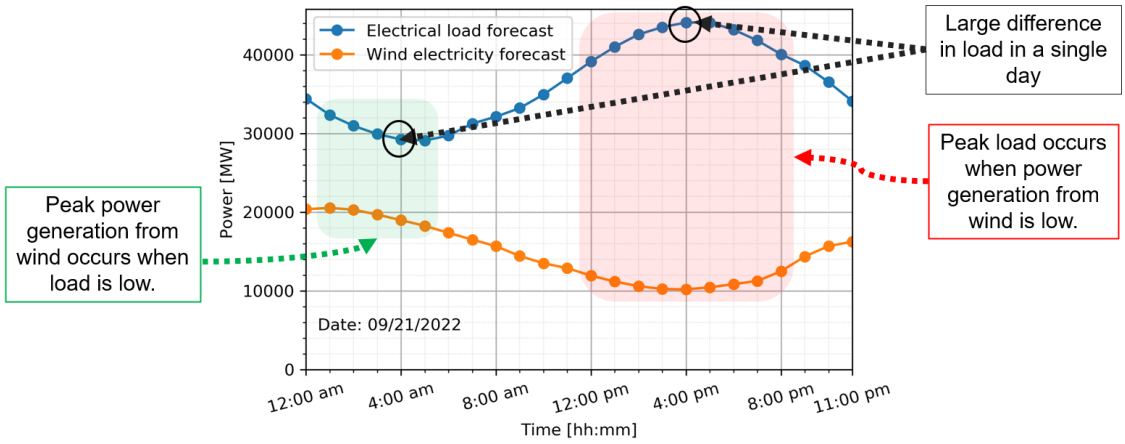

Figure 1.1: Transient nature of load and demand forecast; data source: SPP (2022)

1.2 Literature Review

Many publications are available in open literature on how to integrate renewable energy with building heating and cooling using a thermal energy storage tank. There is not much research work available on three fluid fin and tube heat exchangers. Some of those findings have been mentioned in this chapter.

1.2.1 Different Types of Thermal Energy Storage (TES)

Thermal energy storage can be categorized into two types: sensible and latent thermal energy storage. Different materials are used to store energy depending on the range of operation temperature, storage material, and application [Hasnain (1998a)].

Water is the most used material for sensible TES due to it's low cost and availability [Garg et al. (2012)]. It also has a high heat storage capacity of 4.2 $kJkg^{-1}K^{-1}$,

excellent thermal conductivity, high density, and low viscosity. Water is also non-toxic and non-flammable. Water is a perfect candidate for TES material in residences as it is already available there. Water can be used as phase change material (ice) for cold storage and liquid water for temperatures between 0°C to 100°C. An important parameter for TES performance is thermal stratification. Thermal stratification is the different volumes of TES material in the tank having different temperatures [Alva et al. (2018)]. Thermal stratification increases the performance of a TES system [Cristofari et al. (2003); Hollands and Lightstone (1989)] and water naturally produces thermally stratified TES tanks due to having density differences at different temperatures [Gil et al. (2010)]. Water has a minimum density at 4°C which may affect thermal stratification of the TES tank if operated with a charging temperature below 4°C and a discharging temperature above 4°C, and further work should be done to investigate possible destratification issues in that specific operating condition.

For latent TES, phase change materials (PCM) are used. PCM are generally available in three types: Organic, Inorganic, and Eutectics. One of the major advantages of using PCM is, as they are charged by latent heat, which is much higher than the sensible one, that the TES tank size becomes much smaller. While some researchers state the outlet temperature from the TES tank always stays the same [Alva et al. (2018); Hasnain (1998a); Zhou et al. (2012)], it varies for applications that use encapsulated PCM, e.g. [Novoselac and Bourne (2021)]. PCM also requires a redesign of current heat exchangers in the market as PCM in a solid state creates an insulating layer in the heat exchanger tube [Hasnain (1998a)]. PCMs are generally available in three types: Organic, Inorganic, and Eutectics. Organic PCM can be used for large temperature ranges and are chemically stable. But their disadvantage is they have a very low thermal conductivity of around 0.2 W/m-K at solid phase [Zhou et al. (2012)], and they are also flammable which increases the cost of the TES tank. Organic PCM suitable for residential heating and cooling with a melting

temperature between 20-25°C are Paraffin C16-18 (20 – 22°C), Butyl Stearate(19°C), 1-Dodecanol(26°C), etc. Another PCM material commonly used is salt hydrates. Salt hydrates like KF.4H2O(18.5°C), and Mn(NO3).6H2O(25.8°C) can potentially be used in residential heating and cooling. They have higher thermal conductivity compared to the organic PCMs and lower volume change [Zhou et al. (2012)]. The salt hydrate PCM suffers from supercooling [Al-Shannaq et al. (2015)] which causes the PCM sometime to get cooled without changing phase. This undesirable property reduces the capacity of the PCM material the TES.

For our project, we have selected water as a TES material rather than PCM. Even though PCM has several desirable properties like higher capacity, each PCM material can be used for only a certain temperature [Zhou et al. (2012)] while water can be used for temperatures between 0 to 100°C. Alghamdi (2022) found the minimum size of water-based TES to be 4.5% of the house's footprint, which makes it comparable to PCM-based TES. With water as TES material, we can use regular hydronic heat exchangers available in the market.

1.2.2 Integration of TES with Building Heating and Cooling

Le et al. (2019) developed a TRANSYS model of a heat pump integrated with TES to replace a fossil fuel boiler and validated the model with field data. The heat pump and TES have three different operation modes which is direct, storage or buffer, and combined mode. During direct mode, the heat pump works standalone without the TES and during storage mode, the heat pump keeps charging the TES between 65° and 75°C. In the combined mode, the TES supplied the hot water to the house and as soon as the TES temperature dropped below 55° C, the heat pump would take over. The running costs of all three modes were higher than a 90% efficient gas boiler but the carbon emission were much lower. The heat pump gives the best performance during direct mode and the worst performance during storage mode.

Kim et al. (2018) developed an experimental setup for a heat pump integrated with TES. In their setup, some of the refrigerants were bypassed to the TES during regular operation. As mass flow into the TES increases, the charging time gets reduced. They tried to find the optimum mass flow ratio which will give the highest COP. During discharge, the TES will work as a second evaporator for the heat pump. Some of the refrigerants will get higher capacity from TES as TES will have a higher temperature than outdoor. This will decrease the compressor work and increase the COP. The authors tried to find the optimum discharge mass flow ratio to get the best COP possible.

One of the most used TES systems in the cooling application is Chilled Water Thermal Energy Storage Tank (CWTS). The efficiency of the CWTS system depends on the thermal stratification of chilled water inside the tank [Hasnain (1998b)]. Sebzali et al. (2014) retrofitted a central chilled water plant with a CWTS and evaluated the economic performance of three different control strategies. In the load-leveling control scheme, the CWTS charges when the demand is less than the chiller capacity and discharges when the demand is higher than the chiller capacity while the chiller is running at full capacity. In the 50% demand limiting control strategy, the chiller runs at half capacity during the peak load while the CWTS supplies the rest of the cooling load. In the full storage strategy, the chiller remains completely shut down during peak load and the CWTS supplies the full cooling load to the plant. Annually load leveling, 50% demand limiting, and full storage control strategy provide 6.9%, 9.1%, and 5.0% less energy consumption for the chiller accordingly.

Mokarram and Wang (2022) developed an ice storage thermal system with a novel three-fluid microchannel evaporator. The evaporator has water and refrigerant flowing in parallel while the air flows in a cross-flow direction. During off-peak hours, the water gets supercooled in the evaporator and produces ice slurry which gets stored in a TES tank. During peak hours, the ice slurry from TES provides additional cooling

with the heat pump to meet demand. For this thesis to integrate TES with heating and cooling, we have decided to use three fluid heat exchangers as well. Heng (2017) explored an efficient heat pump model with two water-based TES tanks along with a ground loop heat exchanger. The water TES tanks act as a source or sink for daily usage and the ground acts as a seasonal TES.

1.2.3 Three Fluid Heat Exchanger (TriCoil™)

The concept of three fluid heat exchangers has been investigated by several researchers. Liang et al. (2022) developed an efficient cooling system with a three-fluid fin and tube heat exchanger as a condenser. The heat exchanger is like a regular fin and tube heat exchanger with each tube having two channels in them that carry the water and refrigerant. The water is connected to a cooling tower to provide a better sink temperature during cooling and helps to increase the efficiency of the overall system. Zhang et al. (2016) also proposed a three-fluid fin and tube heat exchanger where the tubes are concentric, and refrigerant evaporates in the inside tube while water is flowing in the outside tube. Green et al. (1982) submitted a patent for a fin and tube three fluid heat exchanger where some of the tubes have refrigerant and others have water in them and they will transfer heat through fins. The three-fluid heat exchanger named TriCoil™ used in this thesis has a similar concept.

The TriCoil™ heat exchanger thermally connects three fluids: water, refrigerant and air at the same time as shown in Figure 1.2. The difference between the TriCoil™ and a regular heat exchanger is that some of the circuits in TriCoil™ are used for refrigerant and some are used for water. The heat exchange between refrigerant and water is caused by a phenomenon called cross-fin conduction. Cross-fin conduction is the transfer of heat through the fin from one tube to another in a heat exchanger. In general, cross-fin conduction is undesired as it reduces the heat exchanger effectiveness at part load, but in TriCoil™ the cross-fin conduction is used to heat or cool the water

by the refrigerant in the adjacent circuits.

To realize the use of TriCoil™ let's consider a scenario when the heat pump of a building has a maximum capacity of 4 tons. In a time when the cooling/heating demand on the building is less than 4 tons, say 2 tons; the excess 2 tons from the heat pump can be transferred to the water in the TriCoil™ by cross-fin conduction. This water will be stored in a TES for later usage when the cooling/heating demand of the building is high. TriCoil™ has 5 different operation modes.

1. Charging: No airflow, water, and refrigerant circuit will be running. Refrigerant will cool/heat the water which will be stored in a thermal energy storage tank for later usage.

2. Charging and Cooling: All three fluids will be active at the same time. The Refrigerant will be charging water as well as cooling/heating the air depending on the heat pump mode.

3. Cooling/Heating: No water flow and refrigerant will cool/heat the air. This is like a regular heat pump air handler unit (AHU).

4. Discharging: No refrigerant flow and water from the thermal energy storage tank will cool/heat the air. In this mode, TriCoil™ will work like a regular hydronic heat exchanger.

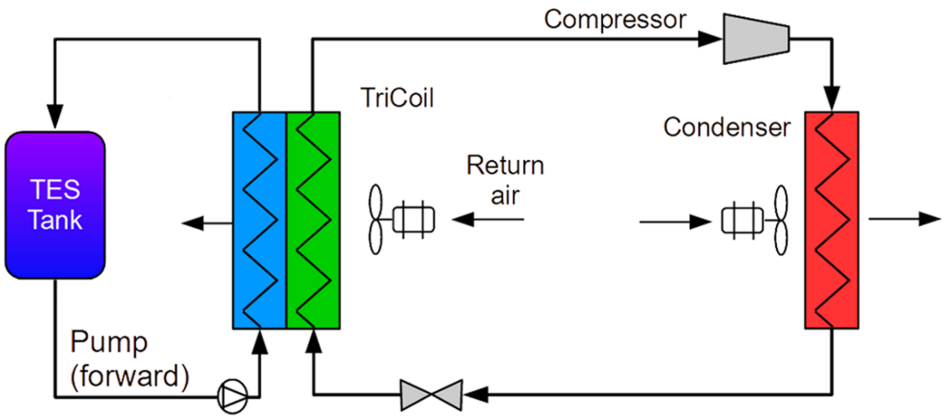

Figure 1.2: Simple schematic of TriCoil™ system [Bach and Spitler (2021)]

TriCoil™ depends on cross-fin conduction to transfer load from refrigerant to water. According to Romero-Méndez et al. (1997) effect of the cross-fin conduction on the total capacity of a heat exchanger increases as the temperature difference between tubes increases. Cross-fin conduction can reduce the total capacity up to 20% according to them. During charging and charging-cooling mode the difference between refrigerant tube and water tube temperature will be high and as such there will be a significant amount of cross-fin conduction which is desirable in our application. OSU has a heat exchanger model called 'xFin' developed by Sarfraz et al. (2019) which takes cross-fin conduction into account. Another Ph.D. student modified the 'xFin' model to support TriCoil™ and use the experimental data from this thesis to validate the TriCoil™ mode. To validate the 'xFin' Sarfraz et al. (2020) tested a heat exchanger with 8 circuits in a wind tunnel with a pumped refrigerant loop. When 7 circuits were active the difference between analysis with no cross-fin conduction and experimental results was a maximum 4%, for 4 active circuits it was 12% and for 3 active circuits, it was 30%. According to Lee and Domanski (1997) cross fin conduction increases with the temperature difference between two adjacent tubes. If both tubes have two-phase fluid, the fin conduction will be lower and fin conduction will be higher if one of them has superheated fluid.

1.2.4 Heat Exchanger Test Setup

Several universities, industries, and national labs have their own wind tunnel for testing heat exchangers. These wind tunnels can be opened or closed. Bell and Groll (2011) used a 2 ft x 2 ft forced flow wind tunnel to compare the pressure drop in airside and heat transfer of microchannel and plate-fin heat exchanger during fouling. A water loop with a heater was connected to the heat exchanger while cold air passed through the heat exchanger in the wind tunnel. It was found that the wavy fin heat exchangers are less affected by fouling than microchannel heat exchangers.

Huisseune et al. (2013) used an open wind tunnel to validate their CFD model for a compound heat exchanger with a louver fin and vortex generator. The heat exchanger is connected to a closed pumped water loop with the water heater. They found out that the louver angle and fin pitch have the most contribution to the friction factor. Albanakis et al. (2009) experimentally tested the effect of different parameters on the pressure drop through a heat recovery heat exchanger for an aero engine. They also used an open wind tunnel with pumped water closed loop. They found out that inlet air temperature and angle of attack play an important role in pressure drop. Marković et al. (2019) used an experimental setup with open wind tunnel and open water loop to develop a friction factor correlation for plate finned tube heat exchanger. De Schampheleire et al. (2013) also used an open wind tunnel and pumped water closed loop to evaluate and compare the performance of the louvered fin heat exchanger and in-house-built aluminum foam fin heat exchanger. The louvered fin heat exchanger performed better at high velocities and contact resistance played an important role in the performance of the aluminum foam fin heat exchanger.

DBM Coils and Padoa University Coils and University (2014) built a wind tunnel to test heat exchangers of a maximum 2.8 ft x 2.8 ft size. It also has a pumped water loop connected to the test heat exchanger. Oak Ridge National Laboratory has a 4 ft x 4 ft wind tunnel with a maximum flow rate of 9000 CFM to test novel heat exchanger concepts. Lee et al. (2010) experimentally evaluated the effect of different parameters i.e: number of tube rows, fin pitch, tube alignment, etc. under frosting conditions. Their experimental setup consists of a closed loop wind tunnel of 3 ft x 1 ft of flow area with a conditioning coil and a pumped water loop with a chiller. The pumped water loop is a mixture of water and glycol. Huang et al. (2020) used a closed loop wind tunnel with a pumped water loop to evaluate the thermal and hydraulic performance of "Compact Bare Tube Heat Exchanger". Their wind tunnel uses a nozzle plan for flow measurement and a hydronic heat exchanger as a conditioning

coil. Saleem et al. (2020) developed a pumped refrigerant loop and wind tunnel to test residential size fin and tube heat exchanger at OSU.

1.3 Project Objective

The purpose of this project is firstly to build a test setup with proper instrumentation for testing TriCoil™ heat exchanger in the wind tunnel, and secondly to do the uncertainty analysis of air, water, and refrigerant side and calculate the heat balance of the test setup. Thirdly to determine LMTD and UA values for different modes of TriCoil™ and lastly to provide experimental data for TriCoil™ model validation.

CHAPTER II

EXISTING EXPERIMENTAL SETUP MODIFICATION

The Psychrometric Coil Testing Facility at OSU has a wind tunnel to test commercial-size heat exchangers. The wind tunnel has two sections, namely the conditioning section, and the test section Figure 2.1. In the conditioning section, there are conditioning coils that are connected to 4 heat pumps with a total cooling capacity of 30 tons at 67° F evaporator temperature. The conditioning section also has a 40 kW electric heater and a 30 kW steam generator. This equipment can be used to fix the properties of the air every time it goes to the test section. The test section houses the test heat exchanger and the proper instrumentation to measure the air properties up and downstream of the heat exchanger. The test section has a flow area of 7 ft (width) by 8 ft (height) Kincheloe et al. (2021).

The hydronic part of the TriCoil™ heat exchanger is connected to a pumped water loop (PWL) up in the mezzanine shown in Figure 2.2. The loop has a 40 kW water heater to increase the temperature of the water and is also connected to a chiller to cool down the water. This loop with help of a PID controller keeps the temperature of the water constant to the inlet of the heat exchanger. By keeping the water inlet temperature and inlet air properties constant, the performance of the heat exchanger can be evaluated by measuring the outlet water temperature and air properties.

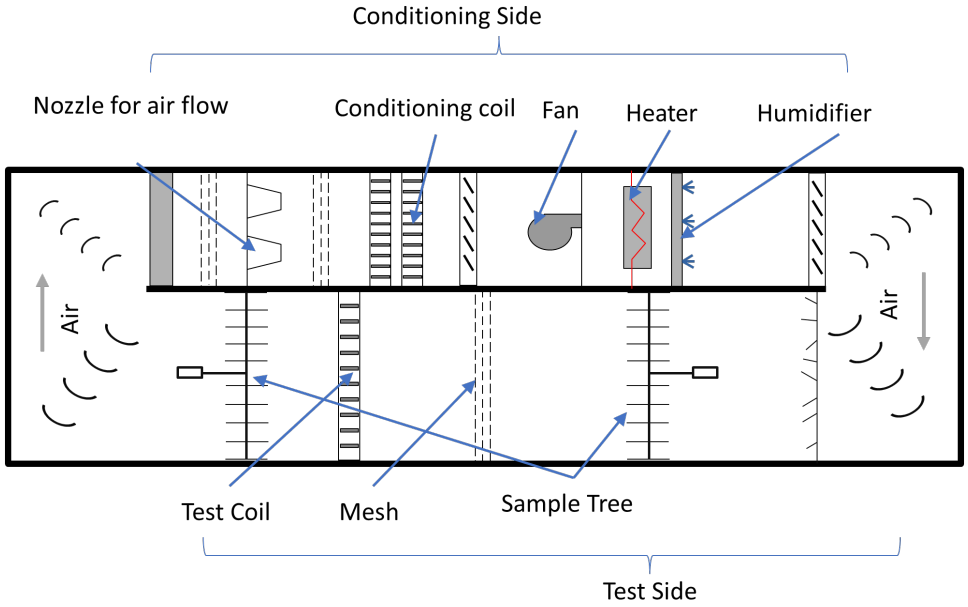

Figure 2.1: Windtunnel at OSU

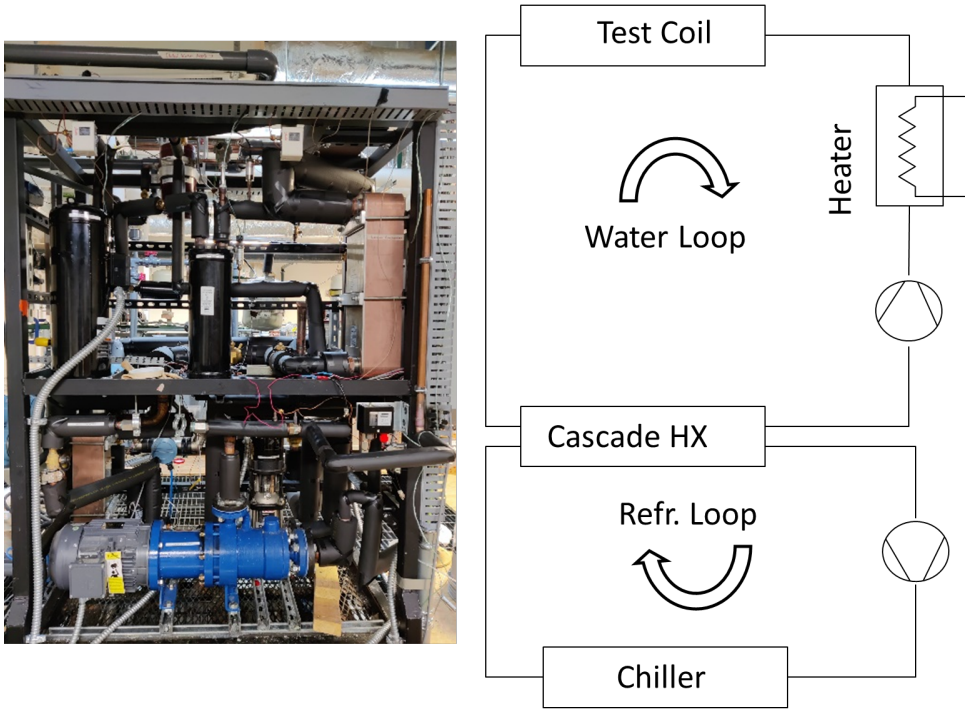

Figure 2.2: Pumped water loop for windtunnel

2.1 Air Heater PID Control

PID control has been set up in LabVIEW VI to control the heater output so that the inlet dry bulb temperature stays constant throughout the test.

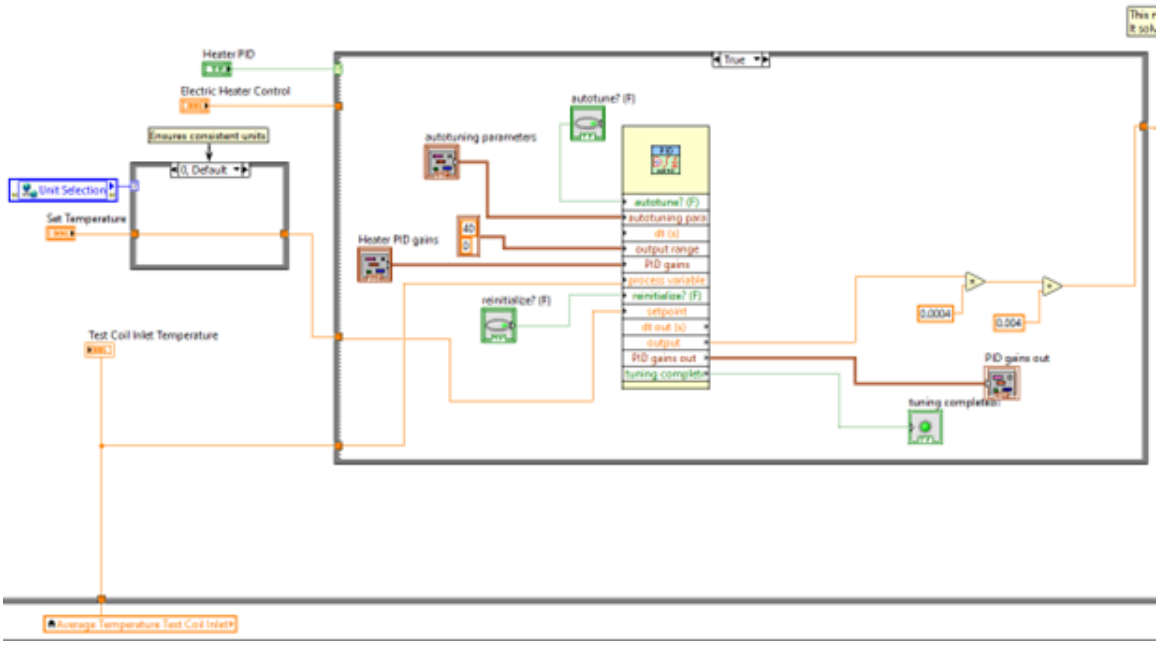

Figure 2.3: Windtunnel heater PID control

The PID control uses the average test coil inlet temperature calculated from a test coil inlet thermocouple grid as the process variable. The tuning factors have been selected by the trial-and-error method.

Table 2.1: Tuning parameters for windtunnel heater PID control

Tuning Parameters	**Value**
Proportional gain	10
Integral time	5 min
Derivative time	0 min

2.2 Steam Humidifier PID Control

Another PID control was set up in the LabVIEW for the steam humidifier to control the humidity of inlet air

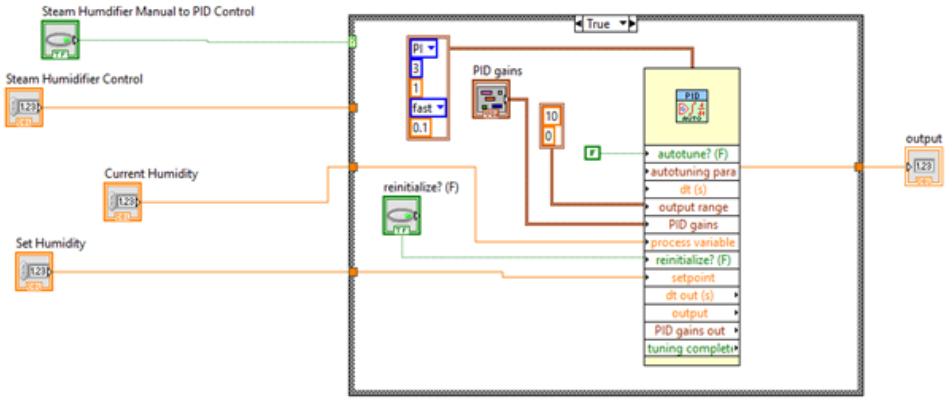

Figure 2.4: Windtunnel steam humidifier PID control

This PID control uses the output from the RH sensor located upstream of the test coil as a process variable. The tuning factors have been selected by the trial-and-error method. The tuning factors have been selected by the trial-and-error method.

Table 2.2: Tuning parameters for windtunnel heater PID control

Tuning Parameters	**Value**
Proportional Gain (Kc)	1
Integral time (Ti)	0.01 min
Derivative time (Td)	0 min

2.3 Water pump VFD Setup

The pumped water loop has a Grundfos pump, and the model number is CRN1-7U-EGJG-EHQQE. This pump was selected by Chowdhury (2021). An ABB ACH580 VFD drive was used to control the pump. The VFD drive requires a 24V digital input to turn on/off the pump and a 0 - 10V analog signal input as a reference to control the speed. The drive itself has a 24V digital output which was connected to the digital input, DI1 of the drive through a relay. The relay coil is activated by an AC transformer. The analog input was provided by a NI module 9266. The 9266 module gives 0 – 20 mA output which was converted to 0 - 10V voltage output by two 1000 Ohm resistant in parallel.

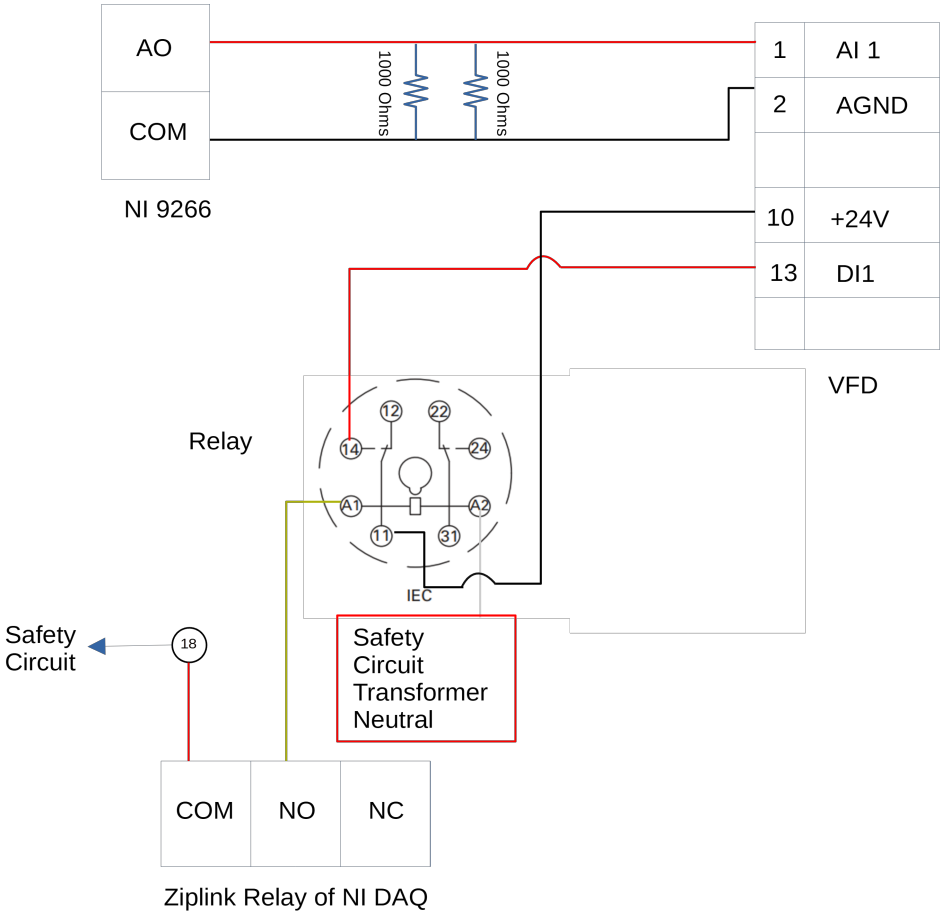

Figure 2.5: Circuit diagram of water pump VFD.

2.4 Water Heater Electrical Connection

We used an SCR to control the output of the heater. The circuit diagram for connecting SCR to the LabVIEW is shown in Figure 2.6.

4 – 20 mA analog output is supplied by LabVIEW to the SCR to control the output of the heater. The SCR has a relay coil that is activated by a transformer through another relay in the PRL safety circuit Chowdhury (2021). The heater requires a 480 V, 3-phase AC power supply.

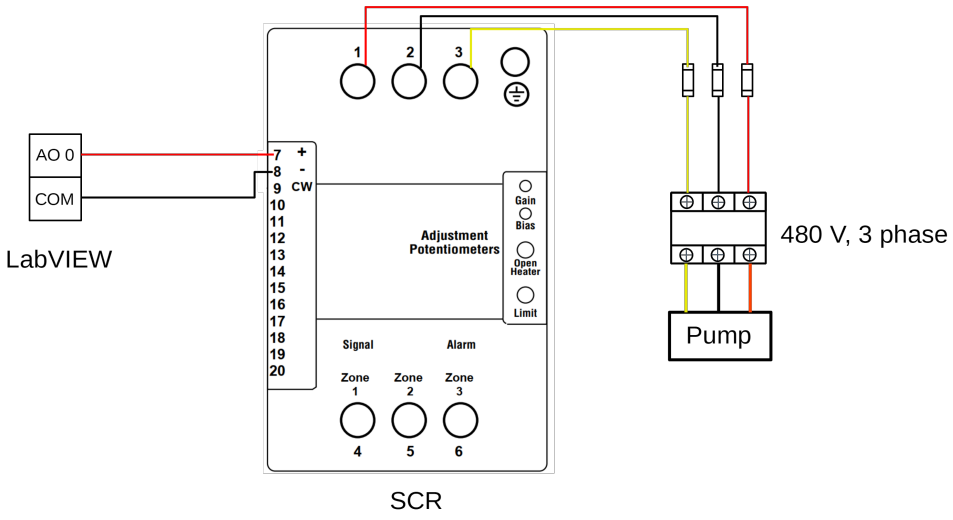

Figure 2.6: Water heater SCR to LabVIEW connection

2.5 Water Heater PID Control

4 – 20 mA analog output is supplied by LabVIEW to the SCR to control the output of the heater. The SCR has a relay coil that is activated by a transformer through another relay in the PRL safety circuit Chowdhury (2021). The heater requires a 480-V, 3-phase AC power supply.

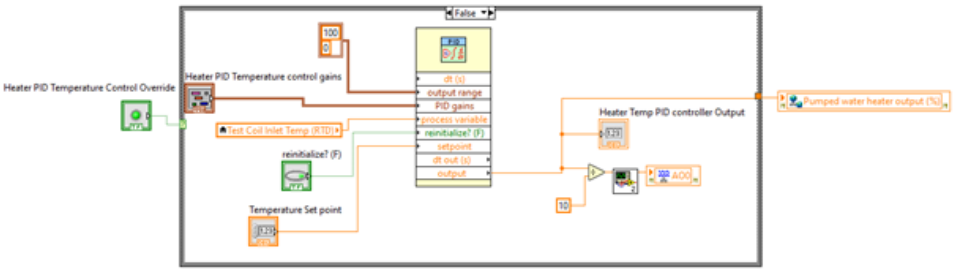

Figure 2.7: Water heater PID control

Test coil inlet temperature is selected as the process variable and the PID gives the percentage of the total capacity of the water heater as output. The tuning factors have been selected by the trial-and-error method.

Table 2.3: Tuning parameters for water heater PID control

Tuning Parameters	**Value**
Proportional Gain (Kc)	1.5
Integral time (Ti)	1.5 min
Derivative time (Td)	0 min

2.6 Water Mass Flow Meter

To measure the mass flow rate of water, a Coriolis mass flow meter from Emerson had been installed by Chowdhury (2021). The mass flow serial no is CMF050M320NRAAEZZZ and the transmitter serial no is 2700R12BBAEZZZ, connected by the following circuit shown in Figure 2.8:

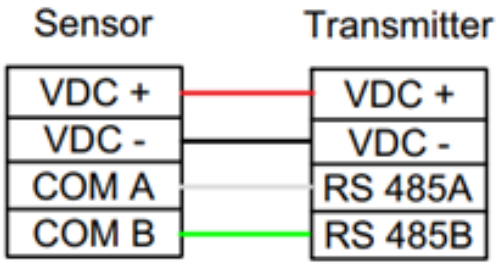

Figure 2.8: Connection between mass flow sensor and transmitter

The transmitter gives 4 – 20 mA output and it was connected to NI 9208 module as shown in Figure 2.9.

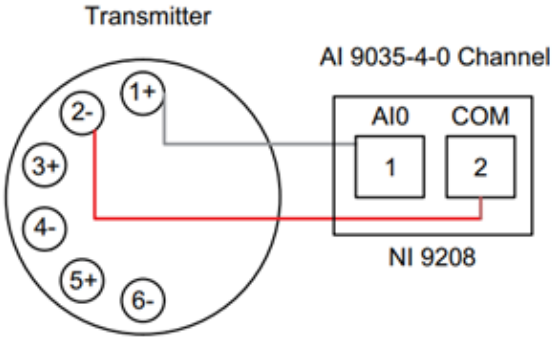

Figure 2.9: Connection between mass flow transmitter and DAQ

CHAPTER III

TRICOIL™ TEST SETUP

The design criteria for the test setup were determined from ASHRAE Standard 33-2016 [ASHRAE (2016)]. The heat balance of the whole test setup needs to be within ±5%. The air leakage needs to stay below 1% at the expected pressure drop during the design air flow rate. The design air flow rate for our test duct is 1600 CFM. The face area of the test coil is 19.6 inches (length) x 34 inches (height). A nozzle plane is required for air flow rate measurement and should be able to measure airflow between 800 and 1600 CFM to facilitate testing with around 2-ton and 4-ton cooling/heating capacity.

3.1 Instrumentation Selection

Instrument selection has been made by following the test results from Bach (2014). Even though a 5-ton heat pump had been used by Bach (2014), his test results should give us a close range of temperature and pressure for a 4-ton heat pump. From Bach (2014), low side pressure and temperature were 114.7 PSI and 2.1°C, and high side temperature and pressure were 364.5 PSI and 72.4°C. The mass flow rate of refrigerant calculated for an equivalent 4-ton system using EES was found to be 156.6 kg/hr. While selecting a mass flow meter, we must also consider zero stability [Emerson (2021)]. The zero stability of a mass flow meter only affects the accuracy when there are either low mass flow rates or higher turndown ratio (Nominal mass flow rate: Mass flow rate). Taking all these into consideration the sensor listed in Table 3.1 have been selected for our test setup:

Table 3.1: Sensor list in TriCoil™ test setup

Sensor Tag	**Sensor Type**	**Location**	**Model**	**Range**	**Manufacturer Uncertainty**
DB1	RTD	Upstream psychrometer of TriCoil	Pyromation R5T185L284-006-12B-13-T3024-0	-30°C to 150°C	± (0.06 + 0.001 —T—) °C
WB1					
DB2	RTD	Downstream psychrometer of TriCoil	Pyromation R5T185L284-006-12B-13-T3024-0	-30°C to 150°C	± (0.06 + 0.001 —T—) °C
WB2					
dPA	Pressure Differential sensor	Nozzle Plane (Code Tester)	Setra 2641-003WD-11-T1-F	0 – 3 in WG	± 0.25% FS
PA1	Pressure Differential Sensor	Inlet of Nozzle Plane	Setra 2641-003WD-11-T1-F	0 – 3 in WG	± 0.25% FS
RH1	RH Sensor	Upstream psychrometer of TriCoil	Dwyer Series RH Humidity Transmitter	0-100% RH	± 2% (10 – 90% RH)
RH2		Downstream psychrometer of TriCoil			

Table 3.1: Sensor list in TriCoil™ test setup

Sensor Tag	**Sensor Type**	**Location**	**Model**	**Range**	**Manufacturer** **Uncertainty**
TR1	RTD	EXV inlet of TriCoil	Pyromation R1T185L284-008-00-15-T3024-0	-200°C to 200°C	± (0.25 + 0.0042 —t—) °C
TR2		TriCoil Refrigerant Outlet	Pyromation R1T185L484-008-00-15-T3024-0		
PR1	Pressure	EXV inlet of TriCoil	Setra 2061500PG2M11028NN	0 –	± 0.13% FS
PR2	Transducer	TriCoil Refrigerant Outlet		500 PSIG	
mR	Coriolis mass flow meter	Refrigerant Mass flow meter	Micro Motion CMF050M320NRAAEZZZ	0 – 6820 kg/h	± 0.10% of flow Zero Stability = 0.078 kg/h

Table 3.1: Sensor list in TriCoil™ test setup

Sensor Tag	**Sensor Type**	**Location**	**Model**	**Range**	**Manufacturer Uncertainty**
TW1	RTD	TriCoil water inlet	Pyromation R1T185L484-008-00-15-T3024-0	-200°C to 200°C	± (0.25 + 0.0042 —t—) °C
TW2		TriCoil water outlet			
PW1	Pressure Transducer	TriCoil water inlet	Setra 2061500PG2M11028NN	0 – 500 PSIG	±0.13% FS
dPW	Differential Pressure Transducer	TriCoil water inlet and outlet	Rosemount 1151DP422B2	0 – 150 in H2O	±0.25% FS
mW	Coriolis mass flow meter	Refrigerant Mass flow meter	Micro Motion CMF050M320NRAAEZZZ	0 – 6820 kg/h	± 0.10% of flow Zero Stability = 0.078 kg/h

3.2 Instrumentation Installation and Calibration

Figure 3.1 shows the position of different instrumentation for TriCoil™ test setup. The refrigerant direction in the Figure is for cooling mode. All the sensors are connected to NI DAQ and LabVIEW VI is used to view and record the data.

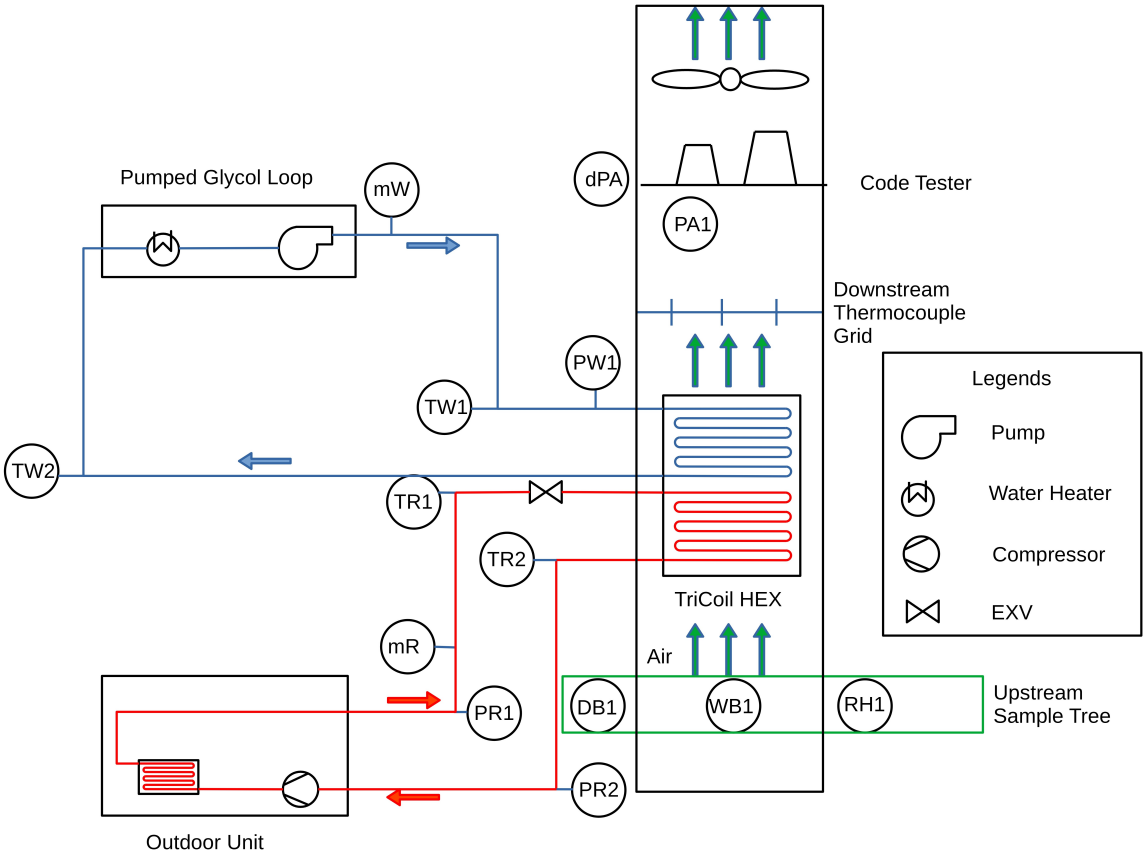

Figure 3.1: TriCoil™ P&ID

The RTD specifications are listed in Table 3.1 and the Pressure transducer's specifications are listed in Table 3.3. Refrigerant mass flow meter specifications are given in Table 3.4

Table 3.2: TriCoil™ test setup's RTD specifcation

Item	**R5T185L284-006-12B-13-T3024-0**	**R1T185L284-008-00-15-T3024-0**	**R1T185L484-008-00-15-T3024-0**
Tags	DB1, WB1, DB2, WB2	TR1	TR2, TW1, TW2
Resistance Type	100 ohm Platinum	100 ohm Platinum	100 ohm Platinum
Temperature Coefficient	0.00385 ohm per °C	0.00385 ohm per °C	0.00385 ohm per °C
Tolerance	(1/5) Class B	Grade B	Grade B
Manufacturer's Rated Accuracy	$\pm(0.06 + 0.001\|T\|)$ °C	$\pm(0.25 + 0.0042\|T\|)$ °C	$\pm(0.25 + 0.0042\|T\|)$ °C
Temperature range	(-30 to 150) °C	(-200 to 200) °C	(-200 to 200) °C
Diameter	1/8 inch	1/8 inch	1/4 inch
Sheath Material	316 Stainless Steel	316 Stainless Steel	316 Stainless Steel
Wire Nos	4 wires	4 wires	4 wires
Sheath Length	6 inches	8 inches	8 inches

Table 3.3: TriCoil™ test setup's pressure transducer's specification

Item	**Item Specification**
Tags	PR1, PR2, PW1
Model	Setra 206
Pressure Range	0 to 500 PSI
Pressure Type	Gauge
Fitting	1/4 inches NPT
Output	4 to 20 mA
Termination	2 ft Cable
Manufacturer's Rated Accuracy	±0.13% FS

Table 3.4: TriCoil™ test setup's refrigerant mass flow meter specification

Item	**Item Specification**
Model	Micro Motion CMF050M320NRAAEZZZ
Nominal Flow rate	3614 kg/h
Maximum Flow rate	6820 kg/h
Zero Stability	0.078 kg/h
Zero Stability Accuracy Equation	$\frac{Zero\ Stability}{Flow\ Rate} \times 100\%$
Manufacturer's Rated Accuracy	±0.10% of rate
Repeatability	0.05% of rate
Output	4 to 20 mA
Transmitter	2700C12BBAEZZZ

Table 3.5: NI cRIO DAQ pinout list for TriCoil™ test setup

Indicator Name	**Tag**	**Signal**	**Chassis**	**Module**	**Module Slot**	**Channel**	**Pinout Code**	**Breakout Box**
TriCoil Refr. EXV Inlet	TR1	RTD	NII 9145(2)	NI 9216	6	4	RTD-91452-6-4	B
TriCoil Refr. Evap Outlet	TR2	RTD	NI 9145(2)	NI 9216	6	7	RTD-91452-6-7	B
TriCoil HX Refr. Inlet Temp		TC	NI 9145(1)	NI 9214	3	15	TC-91451-3-15	A
PRL-Test Coil Inlet Temperature	TW1	RTD	NI 9145(2)	NI 9216	6	5	RTD-91452-6-5	B
PRL-Test Coil Outlet Temperature	TW2	RTD	NI 9145(2)	NI 9216	6	6	RTD-91452-6-6	B

Table 3.5 continued from previous page

Indicator Name	**Tag**	**Signal**	**Chassis**	**Module**	**Module Slot**	**Channel**	**Pinout Code**	**Breakout Box**
Flow Meter For refrigerant loop	mR	4 – 20 mA	NI 9035	NI 9208	4	1	AI-9035-4-1	A
Flow Meter for Glycol loop	mW	4 – 20 mA	NI 9035	NI 9208	4	0	AI-9035-4-0	A
PRL-RL Test Coil Diff. Pressure	dPW	4 – 20 mA	NI 9145(2)	NI 9208	3	0	AI-91452-3-0	A
PRL-RL Test Coil Inlet Pressure	PW1	4 – 20 mA	NI 9145(2)	NI 9208	3	1	AI-91452-3-1	A

Table 3.5 continued from previous page

Indicator Name	**Tag**	**Signal**	**Chassis**	**Module**	**Module Slot**	**Channel**	**Pinout Code**	**Breakout Box**
TriCoil HX Refr. Outlet Pressure	PR1	4 – 20 mA	NI 9035	NI 9208	3	8	AI-9035-3-8	B
TriCoil EXV Refr. Inlet Pressure	PR2	4 – 20 mA	NI 9035	NI 9208	3	9	AI-9035-3-9	B

After connecting the RTDs to the DAQ (Table 3.5), they are calibrated using a reference RTD for temperatures between 10°C and 50°C. From the calibration data, a curve fit equation (Table 3.6) was produced which was used in the LabVIEW VI and heat balance calculations. The accuracy of the reference RTD is ±0.03°C.

Table 3.6: TriCoil™ test setup RTD calibration equation

Sensor Tag	**Calibration Equation**	**Max Calibration Error (°C)**
DB1	0.9974952329848972 * Tdb_in(°C) + (0.03473061679300393)	0.07
WB1	0.9981543447087123 * Twb_in(°C) + (0.003732441167034195)	0.07
DB2	0.9976870975861577 * Tdb_out(°C) + (0.028092673390021083)	0.07
WB2	0.997689171291921 * Twb_out(°C) + (0.03598689026114543)	0.07
TR1	0.999972952401382 * Texv1(°C) + (-0.0055223521113976215)	0.12
TR2	1.0007548611406272 * Tr2(°C) + (0.023601644108540265)	0.08
TW1	1.0000168068328352 * Tw1(°C) + (-0.14257379521926494)	0.07
TW2	0.99971376498684 * Tw2(°C) + (-0.1591037718904902)	0.08

The accuracy of the RTD sensors after calibration is determined using equation 3.1.

$$\text{Accuracy of RTD sensor} = \sqrt{E_{calib,max}^2 + E_{refr}^2} \tag{3.1}$$

Here,

$E_{calib,max}$ = Maximum RTD calibration error = Calibrated Sensor reading - Reference RTD reading

E_{refr} = Reference RTD Accuracy = ±0.03°C

A thermocouple grid has been installed at the outlet of the heat exchanger to measure outlet air dry bulb temperature. There are 15 thermocouples in the grid (Figure 3.2) and their average is taken as the outlet dry bulb temperature. Thermocouple grid accuracy is calculated using Equation 3.2 and found to be ±0.32°C.

$$\text{Accuracy of Thermocouples} = \sqrt{E_{calib,max}^2 + E_{refr}^2 + E_{cj}^2} \tag{3.2}$$

Here,

$E_{calib,max}$ = Maximum TC calibration error = max(Calibrated Sensor reading - Reference RTD reading) = ±0.2°C

E_{refr} = Reference RTD Accuracy = ±0.03°C

E_{cj} = Cold Junction Compensation Accuracy = ±0.25°C

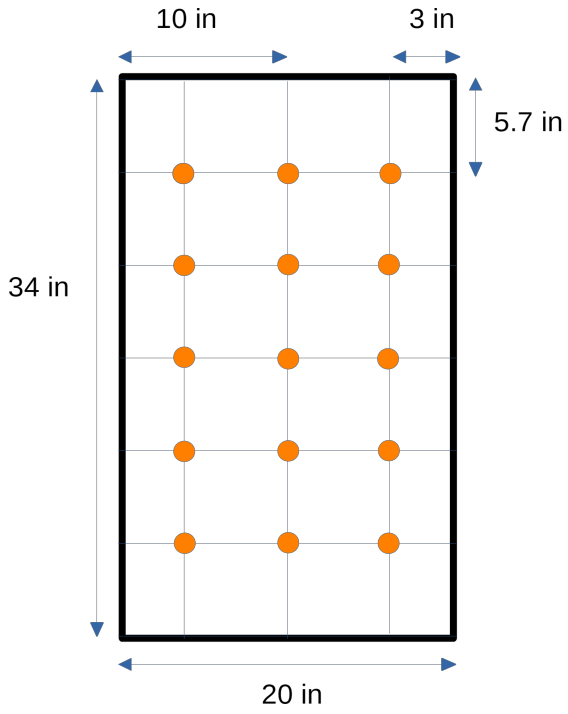

Figure 3.2: TriCoil™ outlet TC grid

3.3 Test Duct Design

While designing the duct Figure 3.3, ASHRAE Standard 41.2-2018 [ASHRAE (2018)] and ASHRAE Standard 33-2016 [ASHRAE (2016)] have been followed. Perforated sheets are placed before the TriCoil heat exchanger and before and after the nozzle to provide uniform flow. Sample Trees are placed upstream and downstream of the heat exchanger for air property measurements. The heat exchanger specifications are

given in Table 3.8. The Duct is made of R-10 $hr \cdot ft^2 \cdot F/BTU$ pink board insulation with 2 in thickness which provides the necessary insulation and structural strength. The nozzle plane (Figure 3.6) has a larger area than the heat exchanger, and for that reason, the upstream and downstream duct has different cross-sectional area. Both ducts are connected by a transition piece (Transitional duct 1 in Figure 3.3). The AHU has an inlet area of 18.635 in x 21.75 which is smaller than the downstream duct area and connected to the duct by another transitional duct piece (Transitional duct 2 in Figure 3.3).

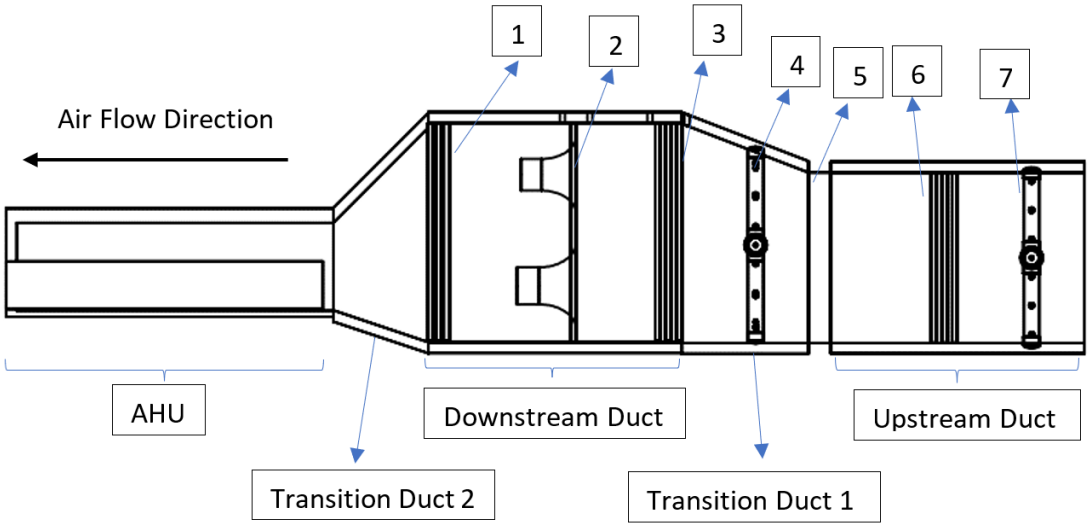

Figure 3.3: TriCoil™ test duct drawing

Table 3.7: Parts of TriCoil™ duct

Nos in Figure 3.3	**TriCoil™ Test duct components**
1	Perforated Sheet
2	Nozzle Plane
3	Perforated Sheet
4	Downstream Sample Tree
5	TriCoilTM Heat Exchanger
6	Perforated Sheet
7	Upstream Sample Tree

3.4 TriCoil™ Heat Exchanger

The TriCoil™ is like a regular fin and tube heat exchanger with the exception that all the circuits in the heat exchanger don't carry only refrigerant or other working fluid. In our experiment, the fin and tube heat exchanger (TriCoil™) 4 out of 8 circuits are connected to refrigerant distributor and carry refrigerant in them while the other 4 circuits are connected to a water header. The detailed circuitry of TriCoil™ is shown in Figure 3.4 and specifications are listed in Table 3.7. The circuit design was done by a Ph.D. student Khaled Alghamdi.

Table 3.8: TriCoil™ heat exchanger specification

Variable	**Value**	**Unit**
Fin density	18	FPI
Tube outer diameter	0.375	Inch
Fin thickness	0.0045	Inch
Coil length	19.6	Inch
Coil height	34	Inch
Coil width	4.19	Inch
Number of banks	4	
Number of tubes	128	Tubes
Column spacing	0.87	Inch
Row spacing	1.00	Inch

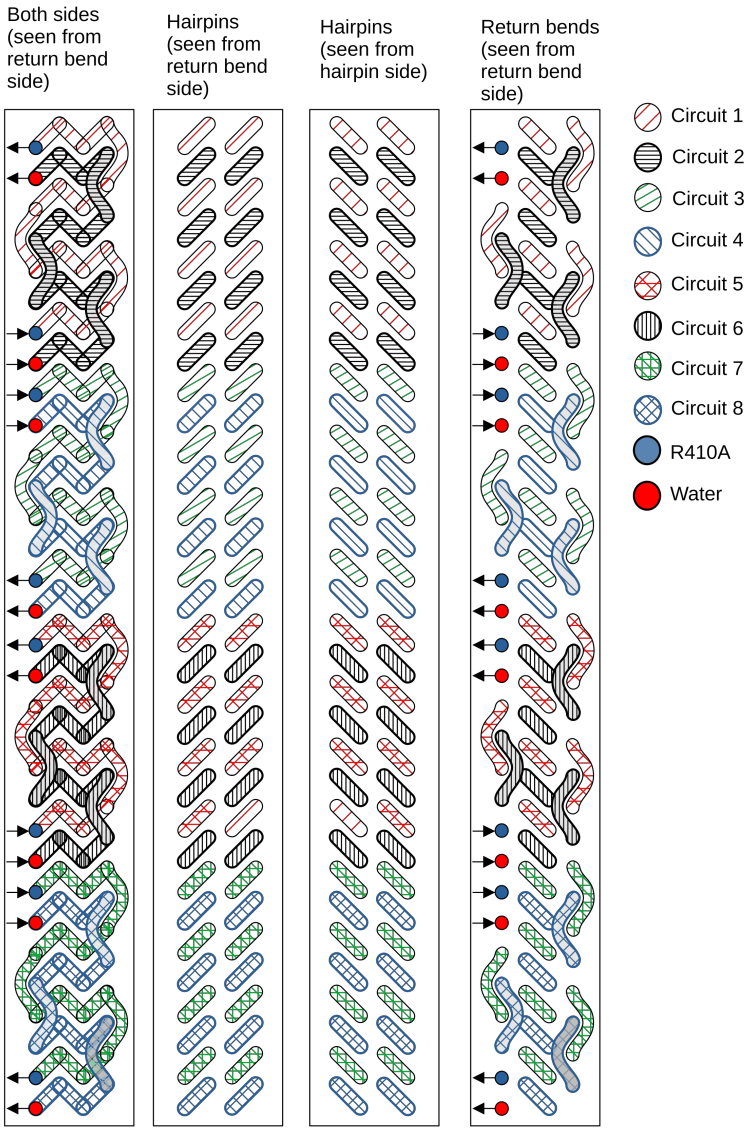

Figure 3.4: TriCoil™ first generation circuit (test coil), credits: Khaled Alghamdi

3.5 Code Tester

To measure the volumetric flow rate of the air we have used a nozzle type flow measurement box according to ASHRAE Standard 41.2 (2018) [ASHRAE (2018)]. While nozzle dimensions selection we were expecting 1600 CFM of airflow for a 4-ton capacity heat pump and 800 CFM for operation with a 2-ton capacity. According to ASHRAE Standard 41.2 (2018) [ASHRAE (2018)], the minimum throat velocity allowed is 3000 fpm while according to ASHRAE Standard 41.2 (1987) [ASHRAE

(1987)], the maximum throat velocity allowed is 7000 fpm. Taking both standard versions into account the following measurable range of airflow has been calculated (Figure 3.5).

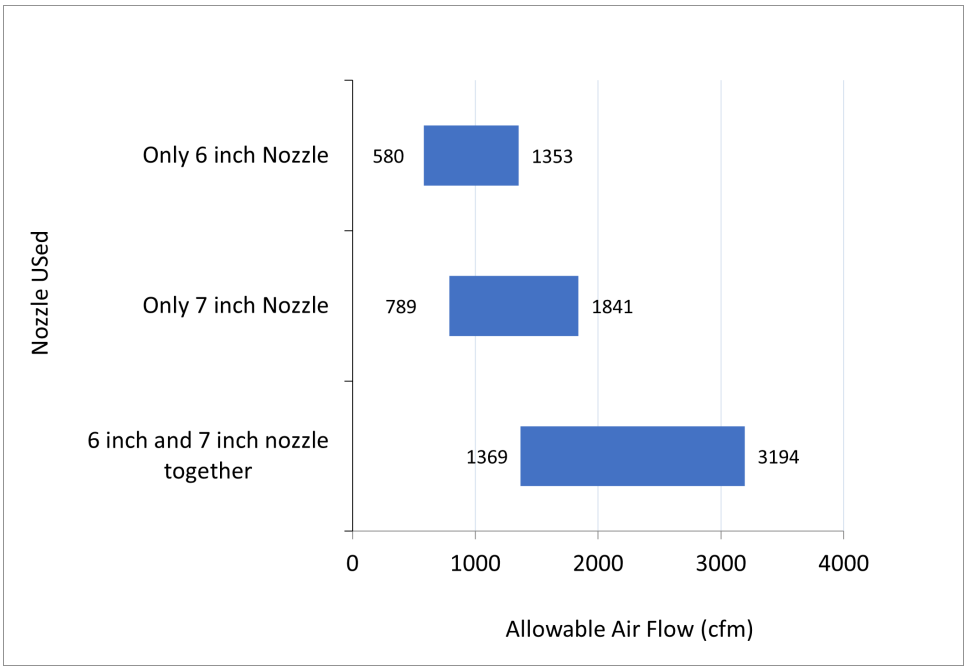

Figure 3.5: Measurable air flow with different nozzle configurations according to ASHRAE Standard 41.2 (2018) and ASHRAE Standard 41.2 (1987)

We have also followed ASHRAE standard 41.2 (2018) [ASHRAE (2018)] while making the nozzle plane. According to the standard, the clear area surrounding the nozzle had to be 3 times its diameter which can be seen in Figure 3.6 of our nozzle plane.

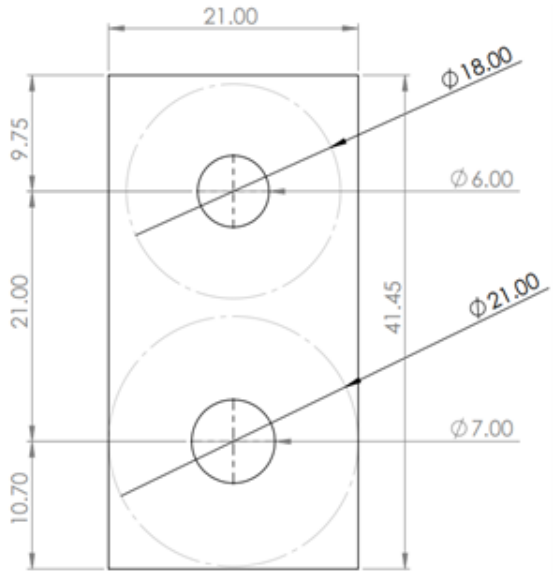

Figure 3.6: Nozzle plane for TriCoil™ test duct (all dimensions are in inches)

3.6 Pressure Drop in The Test Setup

After the selection of nozzle size, the maximum pressure drop inside the duct was calculated to select the Air Handling Unit (AHU). Gan and Riffat (1997) experimentally showed that the pressure drop produced by perforated sheets is equal to the pressure drop of an orifice plate with an equivalent opening area. We have prepared an EES code to calculate the perforated sheet pressure drop using Equation 3.3 for the orifice plate:

$$\dot{Q} = C_d \frac{\pi}{4} D_{orifice}^2 \sqrt{\frac{2\Delta P_{mesh}}{\rho\left(1 - \left(\frac{D_{orifice}}{D_{pipe}}\right)^4\right)}} \tag{3.3}$$

The heat exchanger pressure drop has been estimated from Wen and Ho (2009). From their article, a curve equation (Equation 3.4 has been developed to find out the pressure drop of 2-row plate-fin heat exchangers. The fin density of their heat exchanger was 10 FPI and the tube pattern was 1.000 in x 0.866 in.

$$\Delta P_{hex} = -1.29663893 \times 10^{-2} + 6.32671899 \times 10^{-5}\dot{Q} - 6.36349312 \times 10^{-8}\dot{Q}^2 + 4.40474054 \times 10^{-11}\dot{Q}^3 - 9.09877986 \times 10^{-15}\dot{Q}^4 \quad (3.4)$$

Nozzle pressure drops are calculated from ASHRAE Standard 41.2 (2018) ASHRAE (2018). Equation 3.5 to Equation 3.8 from the standard have been used.

$$Re_d = \frac{\rho_1 V d}{\mu_1} \quad (3.5)$$

$$\epsilon = 1 - 0.548\,(1 - r) \quad (3.6)$$

$$C = 0.99855 - \left[\frac{7.006}{\sqrt{Re_d}}\right] + \left[\frac{134.6}{Re_d}\right] \quad (3.7)$$

$$\dot{Q} = 1097.8 \left[\sum_{i=1}^{N} (C_i A_i)\right] \epsilon \sqrt{\frac{\Delta P_{nozzle}}{\rho_1}} \quad (3.8)$$

Using these equations, we found out the expected pressure drop for different flow rates in the duct (Figure 3.7).

$$\text{Total pressure drop, } \Delta P_{total} = \Delta P_{hex} + \Delta P_{mesh} + \Delta P_{nozzle} \quad (3.9)$$

As the predicted pressure drop in Figure 3.7 is more than 1 in W.G. for 1600 CFM, we have removed the A-coil from the AHU to avoid any unnecessary pressure drop in the duct.

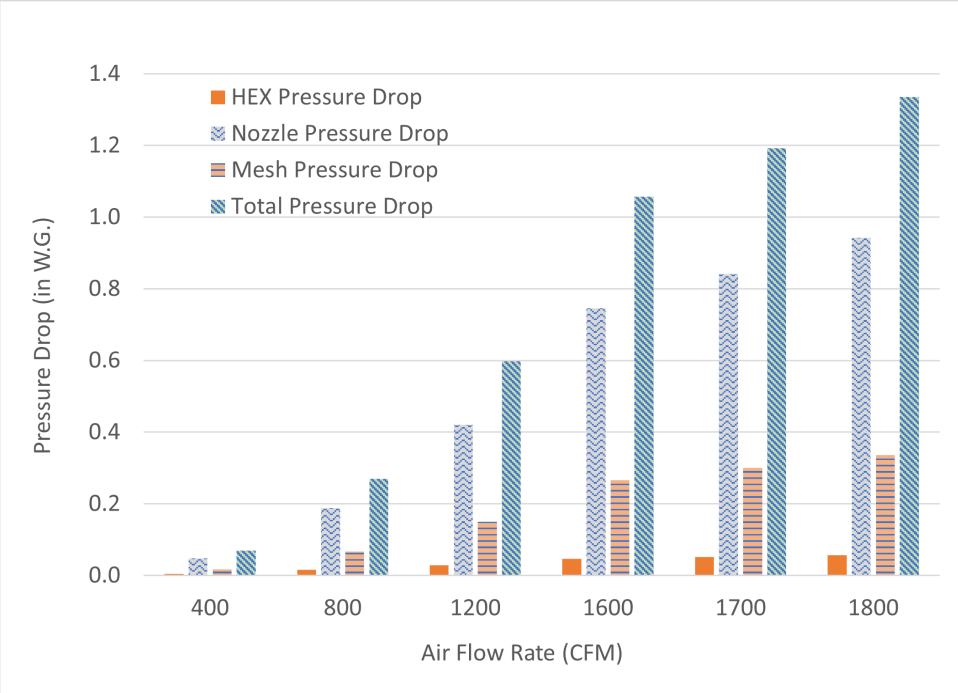

Figure 3.7: Predicted Pressure Drop in the test duct

3.7 Air Handling Unit (AHU) Selection

For building our test setup, Johnson Controls donated an AHU and Outdoor unit. The AHU is York AVV50DE321 [York (2019)]. To use this AHU with our test setup, the AHU fan curve needs to intersect the test duct system curve (Figure 3.8). The AHU has an ECM fan and can provide constant 1760 CFM of air up to 0.5" W.G pressure. The AHU also has an Electronic Expansion Valve (EEV) and EEV controller. The AHU requires 208/230 V, single phase, 60 Hz power supply.

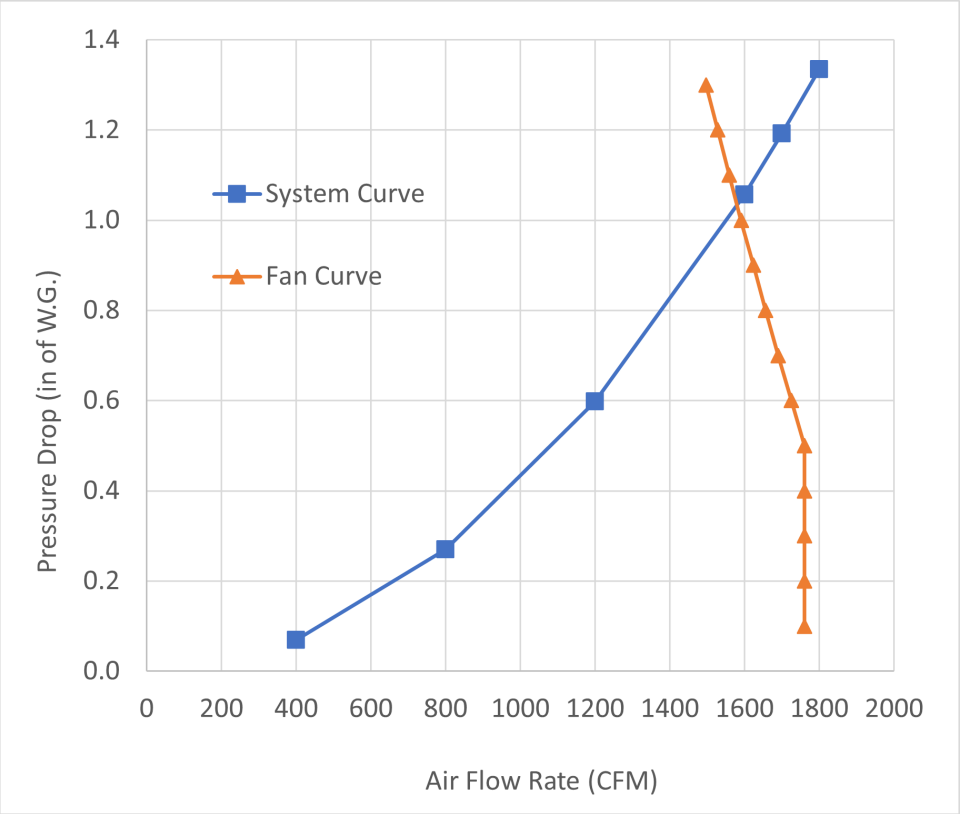

Figure 3.8: TriCoil™ test duct system curve and AHU (York AVV50DE321) fan curve

3.8 Heat Pump Outdoor Unit Selection

The outdoor unit donated by Johnson Controls has model no: York YZV48B21S [York (2017)]. The outdoor unit has a cooling capacity of 4 tons at 23.9°C outdoor temperature and indoor dry bulb temperature of 26.7°C and a wet bulb temperature of 19.4°C. Besides AHU, the outdoor unit also has an EEV which it uses while operating in heating mode.

Table 3.9: York YZV48B21S outdoor unit specifications

Item	**Item Specification**
Unit Supply Voltage	208 – 230 V, single phase, 60 Hz
Compressor Model No	ZPV0342E-2E9-130
Compressor Type	Scroll, Variable Speed
Refrigerant	R-410A
Fan Diameter	26 inches
Fan Motor Rated Power	1/3 HP
Fan motor Rated Current	2.6 Amps
Fan Nominal Speed	975 RPM
Fan Nominal Flow Rate	4800 CFM
Outdoor Coil Face Area	31.2 Sq. ft.
Outdoor Coil Rows	2
Outdoor Fins/inch (FPI)	18
Liquid Line OD	3/8 inches
Vapor Line OD	7/8 inches
Initial Charge	16 lbs.

3.9 AHU, Heat Pump, and Thermostat Setup

A copper tube has been used to connect the outdoor unit with the TriCoil™. The tube sizes are mentioned in Table 3.9. The indoor coil from the AHU has been removed to avoid any unnecessary air pressure drop. The EEV, refrigerant temperature, and pressure sensor of AHU have been relocated to the TriCoil™ for proper operation. We had to use a Johnson Controls Thermostat, HXTM3 S1-THXU430W [Johnson-Controls (2019)] to establish communication between the outdoor unit and AHU. The air handler control box, outdoor unit, and thermostat are connected to each other according to the wiring diagram shown in Figure 3.9. The terminal labels used in Figure 3.9 are explained in Table 3.10.

Table 3.10: Terminal label definition and wire colors [Johnson-Controls (2019)]

Terminal Label	**Signal**	**Definition**	**Wire Color**
A+	Data	Non-inverted signal	Green
R	Low-voltage power hot	24 VAC (Hot)	Red
C	Low-voltage power common	24 VAC (Common)	Black
B -	Data	Inverted signal	Blue / White

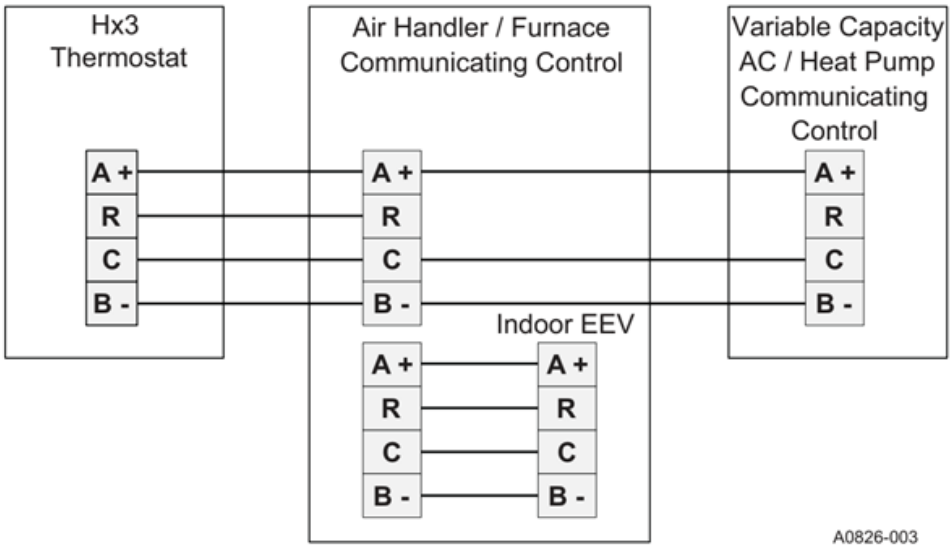

Figure 3.9: Communication wiring diagram for outdoor unit, AHU, and thermostat [Johnson-Controls (2019)]

3.10 Leakage Test of the Test Duct Downstream

A leakage test has been performed on the downstream portion of the duct where the code tester is. From Figure 3.8, it is evident that at 1600 CFM, the expected pressure drop inside the duct will be close to 1" W.G. The leakage rate for 1" of W.G. negative pressure was found to be less than 1% of 1600 CFM (Rated flow rate).

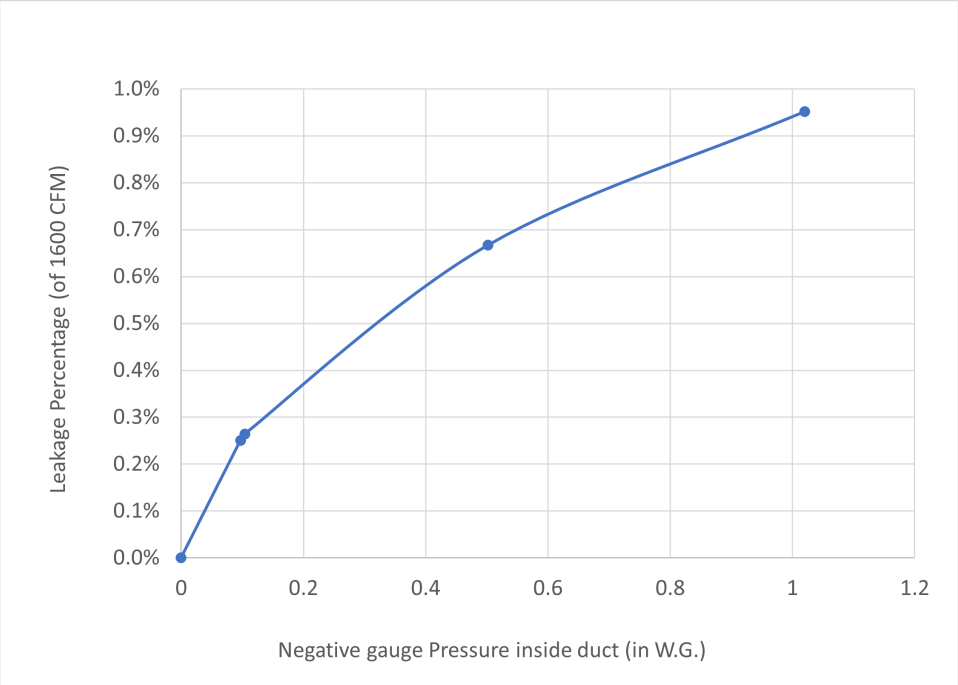

Figure 3.10: Leakage test for the downstream portion of test duct

CHAPTER IV

COMMISSIONING TEST RESULT OF TRICOIL™ TEST SETUP

4.1 Commissioning Test Plan

Test plans for different modes of Tricoil™ have been developed to commission the test setup. We were able to test 4 modes: Cooling, Charging(cooling), discharging(heating), and Cooling-Charging in our test setup. The rest of the modes will be tested later by the new graduate students.

4.1.1 Cooling Mode Test Plan

The test plan for the Cooling test is listed in Table 4.1. In the cooling mode, the TriCoil™ works as a regular indoor coil without the water flow. Two different compressor speeds have been chosen for the full load and partial load test of the setup. The air temperatures were selected to keep the test point inside the compressor operating range. The tests were done at low humidity to keep the coil dry. During writing this report, we were having issues with the downstream/outlet psychrometer and decided to do only dry tests to use the thermocouple grid as dry bulb temperature instrumentation. Each of the test plans has a unique number assigned to them which will be used throughout the report.

Table 4.1: Test plan for TriCoil™ cooling mode

Test plan no	**Air flow (CFM)**	**Compressor Speed (RPM)**	**Inlet air temp (°C)**
C1	800	2040	25.8
C2	800	2040	27.8
C3	1600	3725	25.8
C4	1600	3725	27.8

4.1.2 Charging(cooling) Mode Test Plan

The charging(cooling) mode test plans are listed in Table 4.2. In this mode, the TES water gets heated or cooled depending on the mode of the heat pump. During this test mode, we opened the door of the AHU to bypass the air away from the TriCoil™. In our test, we were only able to cool down the warm water coming from TES or the pumped water loop. To heat the water, we need to cool it down in the conditioning loop to keep the inlet water temperature to TriCoil™ constant. For this, we need the chiller developed by Makhani (2020) which has not been fully commissioned yet. The TES will be emulated by the pumped water loop developed by Chowdhury (2021).

Table 4.2: Test plan for TriCoil™ charging(cooling) mode

Test plan no	Compressor Speed (RPM)	Water mass flow rate (kg/h)	Water inlet temp (°C)
CH1	3725	1700	30.0
CH2	3725	1700	24.0
CH3	3725	1000	30.0
CH5	2040	1700	27.0
CH6	2040	1700	24.0
CH7	2040	1000	27.0
CH8	2040	1000	24.0
CH9	2040	1700	34.0
CH10	2040	1000	34.0
CH11	3725	1760	35.0
CH12	3725	1000	35.0
CH13	3725	1760	18.5
CH14	3725	1760	17.0
CH15	3725	1760	15.0

4.1.3 Discharging(heating) Mode Test Plan

In discharging mode, the TES water provides the cooling or heating for the indoor air while the compressor stays turned off. The test plan for this mode is listed in Table 4.3. We were only able to run the discharging mode in heating as for cooling mode we need the chiller from Makhani (2020).

Table 4.3: Test plan for TriCoil™ discharging(heating) mode

Test Plan no	Air flow (CFM)	Air inlet temp (°C)	Water mass flow rate (kg/h)	Water inlet temp (°C)
D1	800	17.5	1700	41.0
D2	800	17.5	1700	38.0
D3	800	21.2	1700	41.0
D4	800	21.5	1700	38.0
D5	1600	20.5	1700	41.0
D6	1600	20.5	1700	38.0
D7	1600	20.5	800	38.0
D8	1600	20.5	800	41.0
D9	1600	22.5	1700	41.0
D10	1600	22.5	1700	38.0
D11	1600	22.5	800	38.0
D12	1600	22.5	800	41.0

4.1.4 Charging-Cooling Mode Test Plan

In this mode, the heat pump cools the indoor air and charges the TES tank simultaneously. Table 4.4 lists the test plan for this mode. In this test, the heat pump was running at full capacity.

Table 4.4: Test plan for TriCoil™ charging-cooling mode

Test plan no	Air inlet temp (°C)	Water mass flow (kg/h)	Water inlet temp (°C)
CC1	26.0	1700	27.0
CC2	26.0	1700	30.0
CC3	26.0	800	27.0
CC4	26.0	800	30.0
CC5	28.0	1700	27.0
CC6	28.0	1700	30.0
CC7	28.0	800	27.0
CC8	28.0	800	30.0

4.2 Heat Balance

According to ASHRAE Standard 33 [ASHRAE (2016)], the heat balance of the test setup needs to be within ±5%. The heat balance of the cooling mode was calculated

using equation 4.1 from ASHRAE Standard 33.

$$\text{Heat Balance in Cooling mode} = \frac{(|\dot{Q_{sa}}| - |\dot{Q_r}|) \cdot 100\%}{(|\dot{Q_{sa}}| + |\dot{Q_r}|) \cdot 0.5} \tag{4.1}$$

Here,

$\dot{Q_{sa}}$ = Total air sensible capacity

$\dot{Q_r}$ = Total refrigerant side capacity

For discharging (heating) mode, we used the equation 4.2,

$$\text{Heat Balance in Discharging mode} = \frac{(|\dot{Q_{sa}}| - |\dot{Q_w}|) \cdot 100\%}{(|\dot{Q_{sa}}| + |\dot{Q_w}|) \cdot 0.5} \tag{4.2}$$

Here,

$\dot{Q_w}$ = Total water side capacity

For charging (cooling) mode, we used equation 4.3,

$$\text{Heat Balance in Charging mode} = \frac{(|\dot{Q_w}| - |\dot{Q_r}|) \cdot 100\%}{(|\dot{Q_w}| + |\dot{Q_r}|) \cdot 0.5} \tag{4.3}$$

For charging-cooling mode, we used equation 4.4,

$$\text{Heat Balance in Charging-Cooling mode} = \frac{(|\dot{Q_{sa}}| + |\dot{Q_w}| - |\dot{Q_r}|) \cdot 100\%}{(|\dot{Q_{sa}}| + |\dot{Q_w}| + |\dot{Q_r}|) \cdot 0.5} \tag{4.4}$$

Heat balance for different TriCoil™ operation modes and test points are shown in Figure 4.1 to Figure 4.4. In these figures, it can be seen that heat balances for all the test points are within ±5% which validates our test setup according to the ASHRAE Standard 33-2016 [ASHRAE (2016)].

In Figure 4.1, heat balance for the cooling points C3, and C4 is better than C1 and C2 as the test points C3 and C4 are taken at full compressor speed.

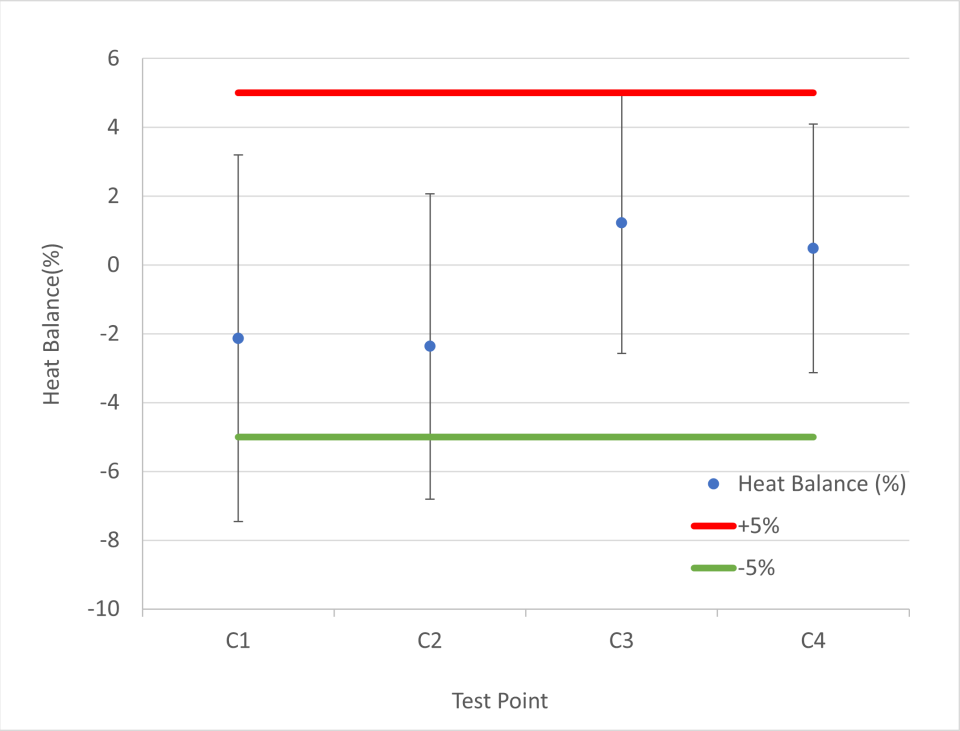

Figure 4.1: Heat balance of test points at cooling mode

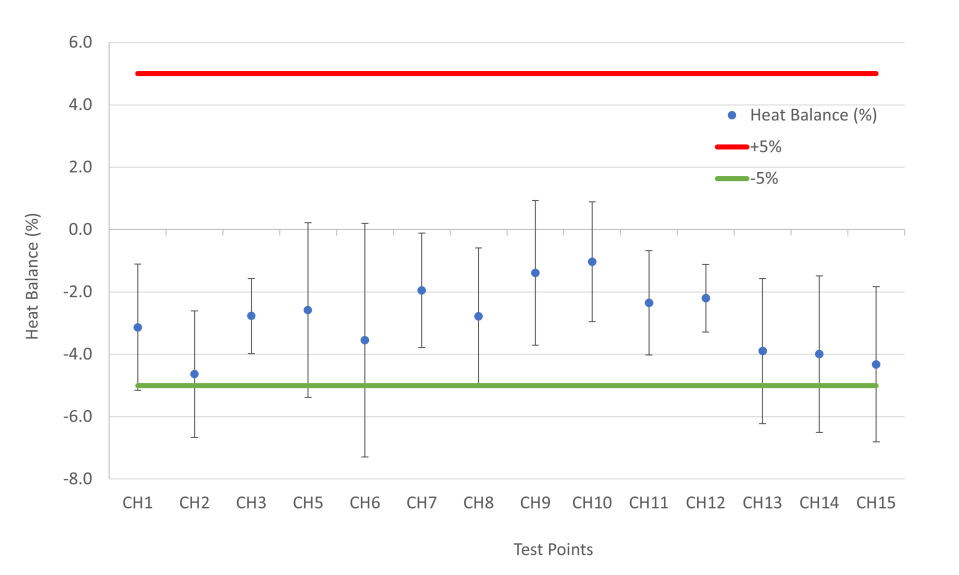

Figure 4.2: Heat balance of test points at charging(cooling) mode

As the capacity goes down, uncertainty in the sensors becomes higher compared to the capacity of the heat exchanger.

In Figure 4.3, heat balance is higher for test points D1 to D4 as the water flow rate is low which also results in a lower capacity. In Figure 4.4 all the test points are

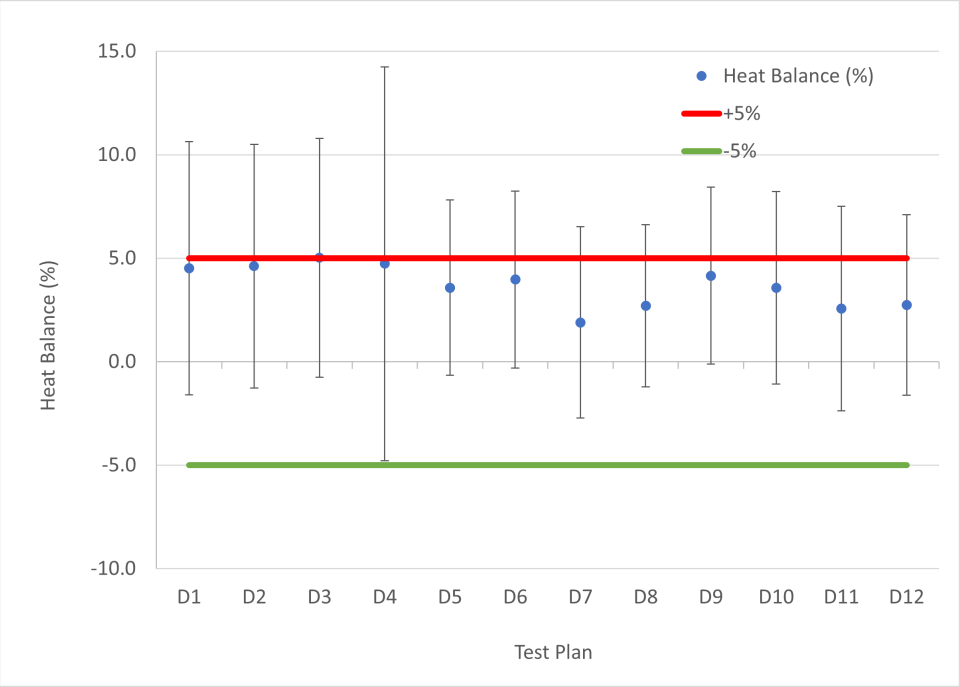

Figure 4.3: Heat balance of test points at discharging(heating) mode

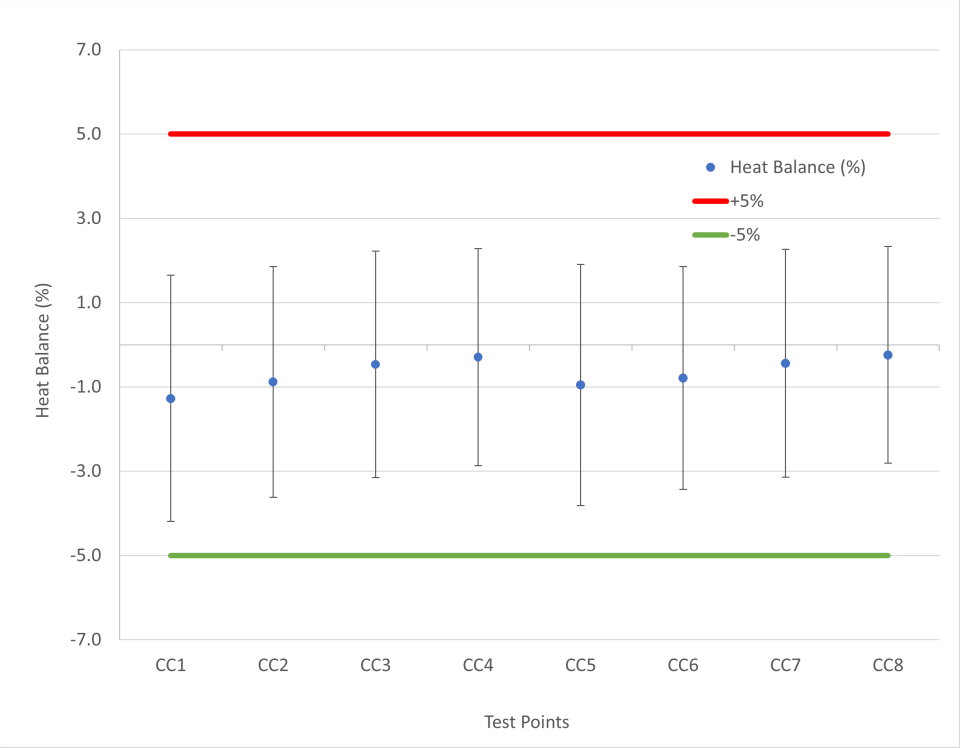

Figure 4.4: Heat balance of test points at charging-cooling mode

running at very high capacity which resulted in a lower heat balance.

4.3 Test Results

Table 4.5: Test results for TriCoil™ cooling mode air side

Test Point	**Dry bulb Inlet (°C)**	**Wet Bulb Inlet (°C)**	**RH Inlet (%)**	**Outlet TC Grid (°C)**	**Air flow rate (CFM)**	**Air Sensible Capacity (kW)**
C1	25.9	12.6	18.9	9.5	824.00	7.36
C2	28.0	13.5	17.1	10.9	828.48	7.63
C3	25.9	12.7	21.8	11.4	1715.74	13.41
C4	27.9	13.7	20.2	12.9	1715.51	13.85

Table 4.6: Test results for TriCoil™ cooling mode refrigerant side

Test Point	**Exv inlet temp (°C)**	**Exv inlet pres. (PSIG)**	**Evap inlet temp (°C)**	**Evap outlet temp (°C)**	**Evap outlet pres. (PSIG)**	**Refr. mass flow (kg/hr)**	**Refr. Capacity (kW)**
C1	24.9	254.67	8.0	13.8	129.46	141.23	7.52
C2	25.5	259.99	9.5	15.2	136.39	147.31	7.81
C3	25.4	254.55	8.9	12.9	126.95	250.86	13.25
C4	26.0	259.19	10.2	14.3	133.12	261.78	13.79

Table 4.7: Test results for TriCoil™ charging(cooling) mode refrigerant side

Test Point	**Exv inlet temp (°C)**	**Exv inlet pres. (PSIG)**	**Evap inlet temp (°C)**	**Evap outlet temp (°C)**	**Evap outlet pres. (PSIG)**	**Refr. mass flow (kg/hr)**	**Refr. Capacity (kW)**
CH1	25.7	252.57	11.8	14.1	141.36	263.35	13.78
CH2	25.5	261.27	7.6	10.6	120.93	240.50	12.60
CH3	24.4	243.75	9.5	12.3	130.68	241.77	12.80
CH5	25.2	255.74	13.5	19.8	159.68	172.81	9.24
CH6	25.6	258.47	11.1	16.9	146.05	157.78	8.37
CH7	25.4	256.24	12.1	17.8	151.51	164.11	8.72
CH8	25.5	256.55	9.6	15.0	138.38	149.78	7.92
CH9	25.6	262.54	17.2	24.5	182.01	195.99	10.53
CH10	25.6	260.85	15.5	22.6	171.39	184.30	9.88
CH11	25.9	253.98	14.3	17.8	155.37	287.45	15.14
CH12	25.2	249.72	12.2	15.6	143.72	265.26	14.04
CH13	24.9	254.39	4.0	7.1	104.56	210.81	11.07
CH14	25.1	255.22	3.2	6.4	101.25	204.07	10.68
CH15	25.4	256.20	2.1	4.6	96.50	195.63	10.16

Table 4.8: Test results for TriCoil™ charging(cooling) mode water side

Test Point	**Water Inlet Temp (°C)**	**Water Inlet Pres. (PSIG)**	**Water Outlet Temp (°C)**	**Water mass flow (kg/h)**	**Water Capacity (kW)**
CH1	29.9	21.91	23.4	1768.73	13.35
CH2	23.8	20.88	18.0	1777.67	12.03
CH3	29.9	20.72	19.7	1060.20	12.45
CH5	27.9	21.24	23.5	1766.29	9.00
CH6	23.9	20.66	20.0	1773.32	8.08
CH7	27.9	18.43	21.0	1065.75	8.55
CH8	23.8	18.27	17.7	1070.11	7.70
CH9	33.9	21.81	28.8	1763.24	10.38
CH10	33.8	18.85	25.9	1062.33	9.78
CH11	34.9	22.25	27.7	1770.31	14.79
CH12	34.8	21.36	23.6	1054.84	13.73
CH13	18.5	19.56	13.3	1784.75	10.64
CH14	17.1	19.56	12.2	1784.48	10.27
CH15	15.0	19.51	10.3	1784.28	9.73

Table 4.9: Test results for TriCoil™ discharging(heating) mode air side

Test Point	**Dry bulb Inlet (°C)**	**Wet Bulb Inlet (°C)**	**RH Inlet (%)**	**Outlet TC Grid (°C)**	**Air flow rate (CFM)**	**Air Sensible Capacity (kW)**
D1	17.6	11.1	44.7	37.3	838.71	8.99
D2	17.5	11.3	46.3	34.8	839.99	7.85
D3	21.7	12.3	35.1	38.0	843.02	7.34
D4	21.6	12.3	34.1	35.5	840.96	6.23
D5	22.7	11.1	15.5	35.1	1723.38	11.88
D6	20.6	11.8	30.8	32.4	1759.43	11.31
D7	20.5	10.1	17.4	29.9	1728.25	9.11
D8	20.6	10.1	17.1	31.7	1720.64	10.64
D9	22.7	13.0	30.2	35.2	1750.93	11.80
D10	22.2	13.0	31.5	32.9	1754.54	10.13
D11	22.6	11.1	15.7	30.9	1729.96	8.00
D12	22.7	11.0	15.6	32.6	1726.08	9.56

Table 4.10: Test results for TriCoil™ discharging(heating) mode water side

Test Point	**Water Inlet Temp (°C)**	**Water Inlet Pres. (PSIG)**	**Water Outlet Temp (°C)**	**Water mass flow (kg/h)**	**Water Capacity (kW)**
D1	40.9	22.22	36.7	1762.84	8.59
D2	37.9	21.87	34.2	1763.22	7.50
D3	40.9	22.34	37.5	1762.33	6.98
D4	37.9	22.1	35.0	1762.49	5.94
D5	40.9	20.74	35.3	1764.29	11.47
D6	37.9	21.14	32.6	1766.10	10.87
D7	37.9	17.04	28.7	835.95	8.94
D8	40.9	17.39	30.2	834.30	10.35
D9	40.9	21.72	35.3	1764.14	11.32
D10	37.8	21.29	33.1	1764.75	9.78
D11	37.9	17.29	29.8	835.20	7.79
D12	40.9	17.53	31.2	833.56	9.30

Table 4.11: Test results for TriCoil™ charging-cooling mode air side

Test Point	**Dry bulb Inlet (°C)**	**Wet Bulb Inlet (°C)**	**RH Inlet (%)**	**Outlet TC Grid (°C)**	**Air flow rate (CFM)**	**Air Sensible Capacity (kW)**
CC1	26.0	12.3	12.7	18.7	1762.09	7.01
CC2	26.0	12.4	12.8	20.4	1758.49	5.38
CC3	25.9	11.8	13.1	17.0	1761.91	8.48
CC4	25.9	12.0	14.0	18.3	1762.09	7.28
CC5	28.0	13.6	17.1	19.1	1692.48	8.16
CC6	28.0	13.7	17.1	20.8	1688.93	6.61
CC7	27.9	13.7	17.2	17.5	1683.89	9.45
CC8	28.0	13.7	17.1	18.8	1686.17	8.30

Table 4.12: Test results for TriCoil™ charging-cooling mode water side

Test Point	**Water Inlet Temp (°C)**	**Water Inlet Pres. (PSIG)**	**Water Outlet Temp (°C)**	**Water mass flow (kg/h)**	**Water Capacity (kW)**
CC1	26.9	19.86	22.9	1773.16	8.08
CC2	29.9	20.2	24.9	1772.18	10.2
CC3	26.9	16.15	20.7	841.02	5.99
CC4	29.9	16.31	22.0	839.56	7.63
CC5	26.8	20.19	23.3	1773.09	7.22
CC6	29.8	20.52	25.3	1772.78	9.28
CC7	26.9	16.68	21.4	836.98	5.33
CC8	29.9	16.88	22.7	835.44	6.97

Table 4.13: Test results for TriCoil™ charging-cooling mode refrigerant side

Test Point	**Exv inlet temp (°C)**	**Exv inlet pres. (PSIG)**	**Evap inlet temp (°C)**	**Evap outlet temp (°C)**	**Evap outlet pres. (PSIG)**	**Refr. mass flow (kg/hr)**	**Refr. Capacity (kW)**
CC1	26.4	269.93	13.0	16.2	146.76	291.63	15.28
CC2	27.0	275.3	14.0	17.7	151.86	300.49	15.72
CC3	27.7	278.96	12.2	15.3	141.84	281.06	14.54
CC4	27.5	277.79	12.8	16.3	145.41	287.64	14.96
CC5	26.3	270.89	13.5	16.8	149.24	295.71	15.52
CC6	26.7	274.43	14.4	18.5	154.43	304.38	16.01
CC7	27.2	276.94	12.7	16.1	144.29	285.08	14.85
CC8	27.0	276.08	13.4	17.0	148.27	292.81	15.30

4.4 Uncertainty Analysis

For uncertainty analysis, ASME PTC 19.1-2013 [ASME (2013)] has been followed. According to the standard, the total uncertainty of a measured variable is determined using Equation 4.5. In Equation 4.5, the systematic uncertainty is determined from the manufacturer manual, and the random uncertainty is determined using Equation 4.6.

$$u_{\bar{x}} = \sqrt{(b_{\bar{x}})^2 + (s_{\bar{x}})^2} \tag{4.5}$$

Here,

$u_{\bar{x}}$ = Total uncertainty of the measured variable

$b_{\bar{x}}$ = Systematic uncertainty of the measured variable

$s_{\bar{x}}$ = Random uncertainty of the measured variable

$$s_{\bar{x}} = 2 \cdot \sigma \tag{4.6}$$

Here,

σ = Standard deviation of a measurement

To determine the uncertainty of the calculated variable, we have used Equation 4.7. The standard deviation has been taken two times in Equation 4.6 to cover a 95% confidence interval.

$$\Delta f = \sqrt{\left(\frac{\delta f}{\delta x_1}\Delta x_1\right)^2 + \left(\frac{\delta f}{\delta x_2}\Delta x_2\right)^2 + \ldots + \left(\frac{\delta f}{\delta x_n}\Delta x_n\right)^2} \tag{4.7}$$

Here,

f = function of x_1, x_2, ..., x_n

The contribution of different measured variables are also calculated and shown in figures from 4.5 to 4.28.

Some of the things that have been observed from the uncertainty analysis is:

1. Pressure difference between the upstream and downstream of the nozzle plane has the highest contribution (around 53 %) for the air flow rate uncertainty which results in the pressure difference also having a substantial contribution (around 29 %) in air sensible capacity calculation.

2. The inlet and outlet temperature uncertainties are the highest contributors to water capacity calculation.

3. Uncertainties in refrigerant mass flow rate and evaporator outlet temperature is the highest contributor to refrigerant capacity calculation.

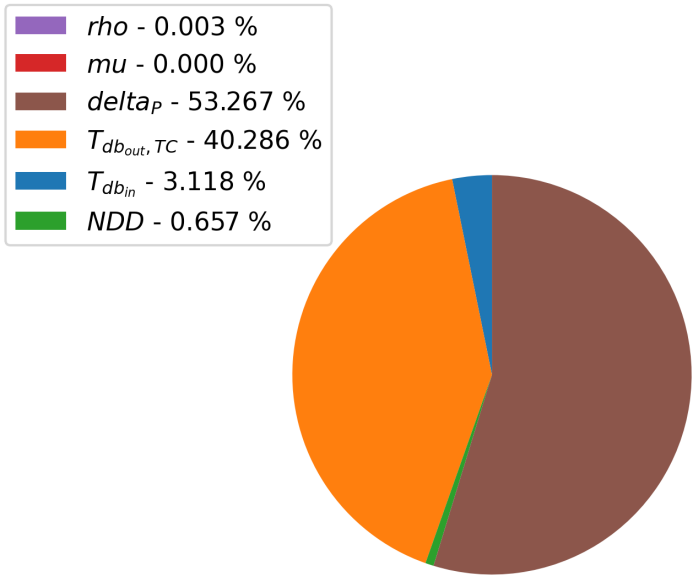

Figure 4.5: Contribution of different variables in calculating air sensible capacity for cooling test point C3

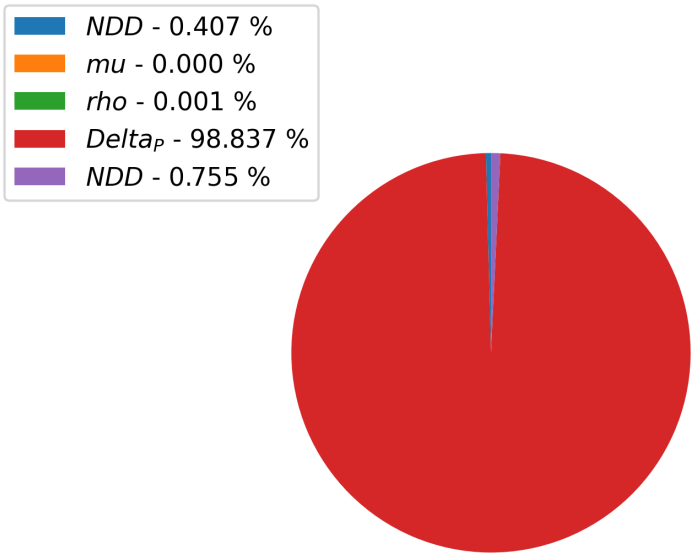

Figure 4.6: Contribution of different variables in calculating air flow rate for cooling test point C3

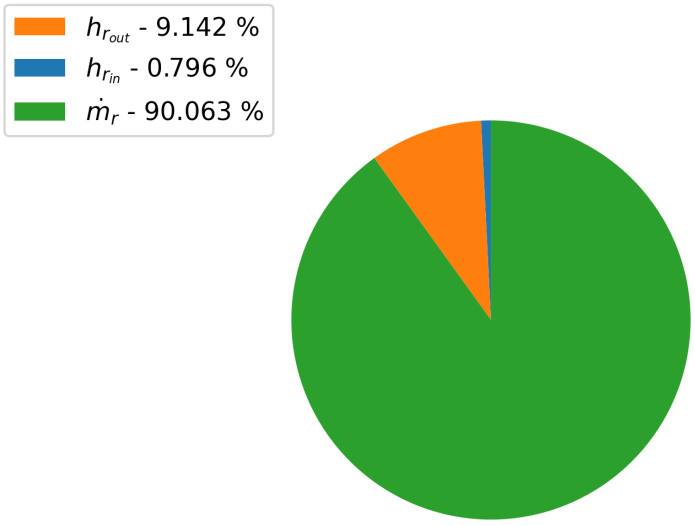

Figure 4.7: Contribution of different variables in calculating refrigerant capacity for cooling test point C3

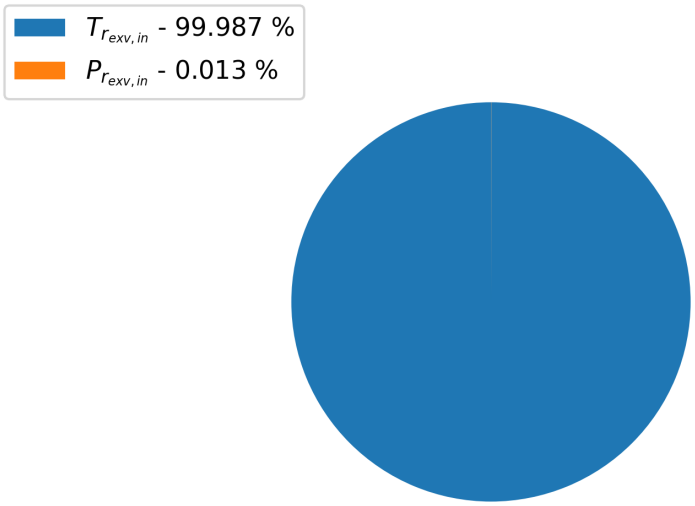

Figure 4.8: Contribution of different variables in calculating refrigerant inlet enthalpy for cooling test point C3

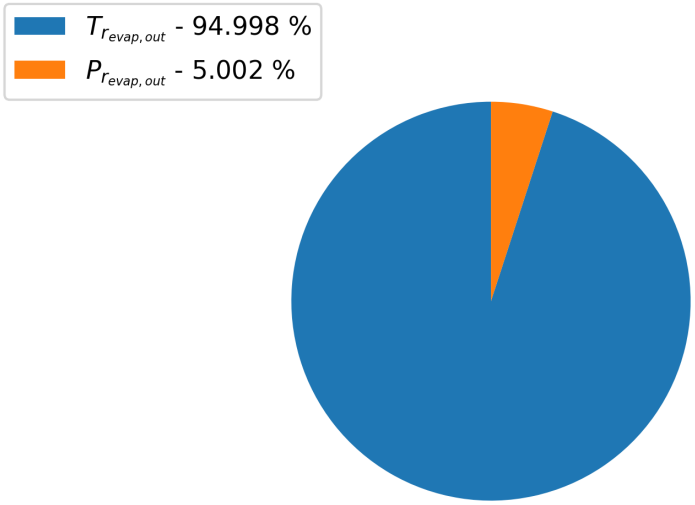

Figure 4.9: Contribution of different variables in calculating refrigerant outlet enthalpy for cooling test point C3

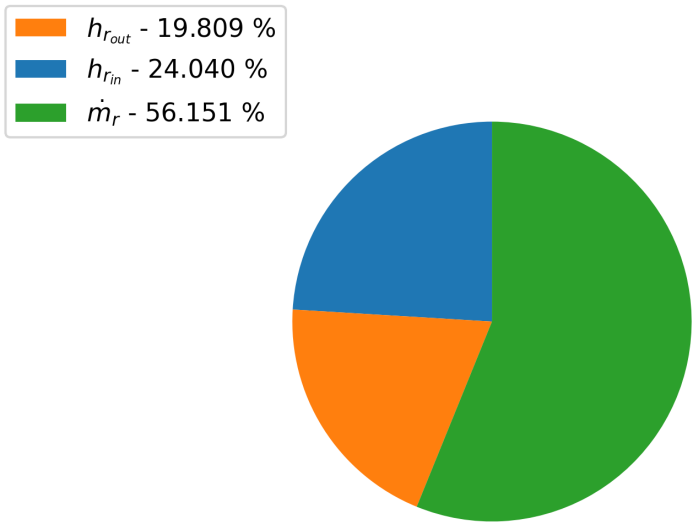

Figure 4.10: Contribution of different variables in calculating refrigerant capacity for charging(cooling) test point CH11

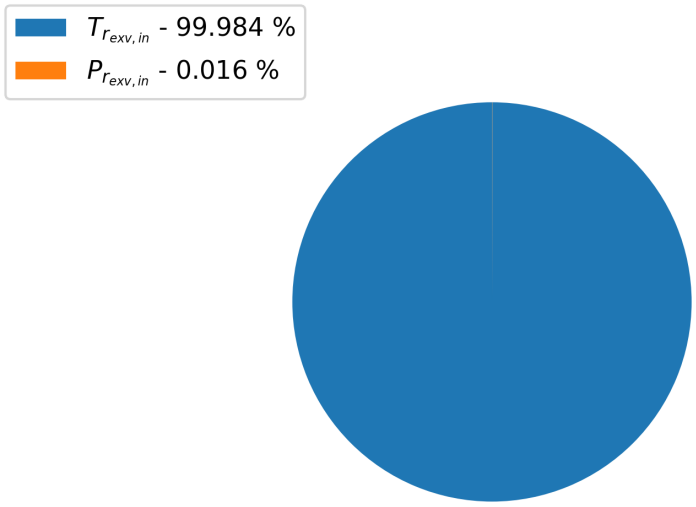

Figure 4.11: Contribution of different variables in calculating refrigerant inlet enthalpy for charging(cooling) test point CH11

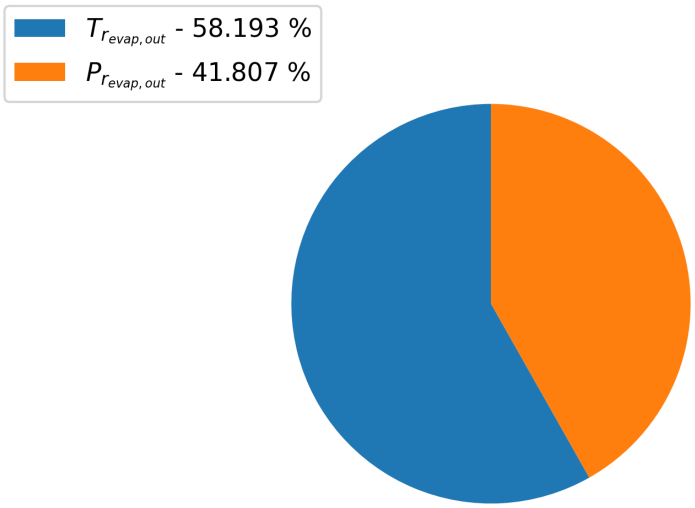

Figure 4.12: Contribution of different variables in calculating refrigerant outlet enthalpy for charging(cooling) test point CH11

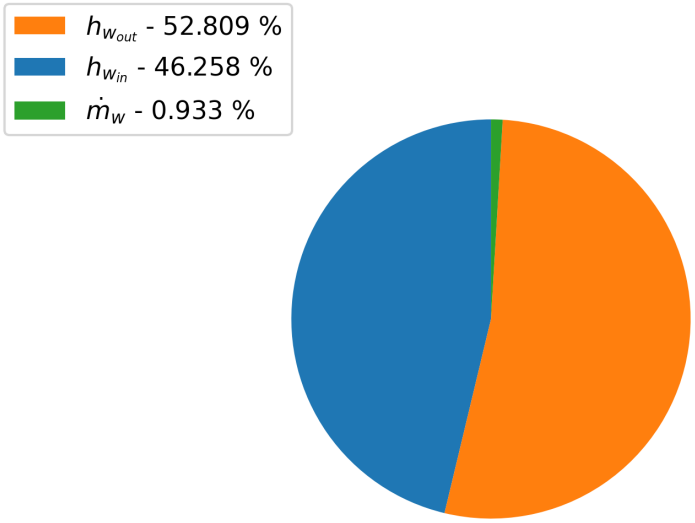

Figure 4.13: Contribution of different variables in calculating water capacity for charging(cooling) test point CH11

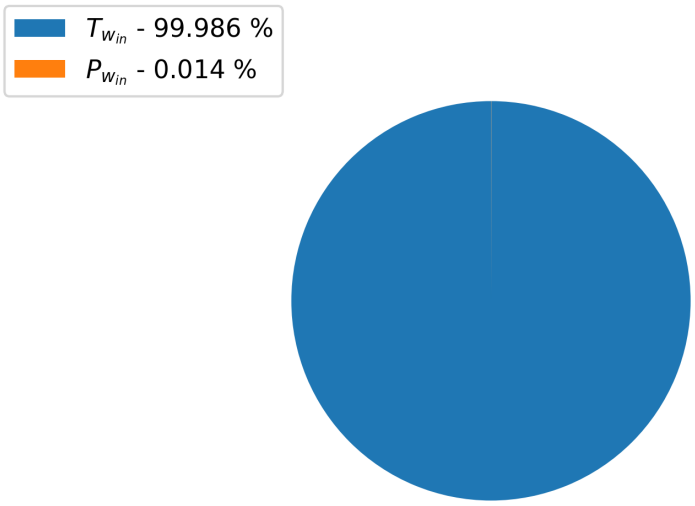

Figure 4.14: Contribution of different variables in calculating water inlet enthalpy for charging(cooling) test point CH11

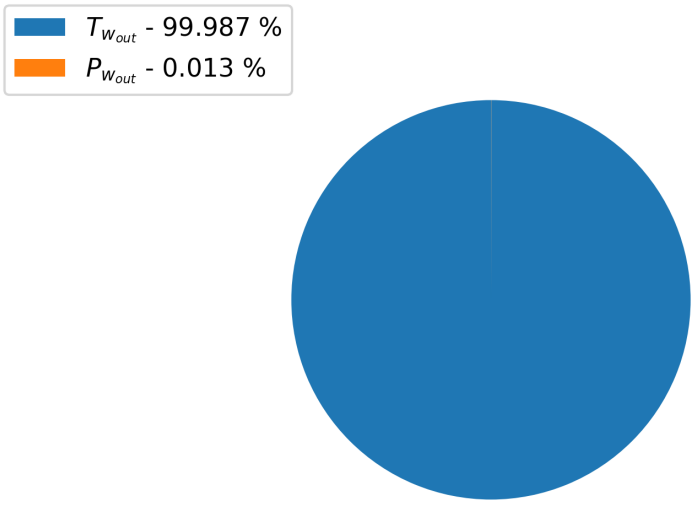

Figure 4.15: Contribution of different variables in calculating water outlet enthalpy for charging(cooling) test point CH11

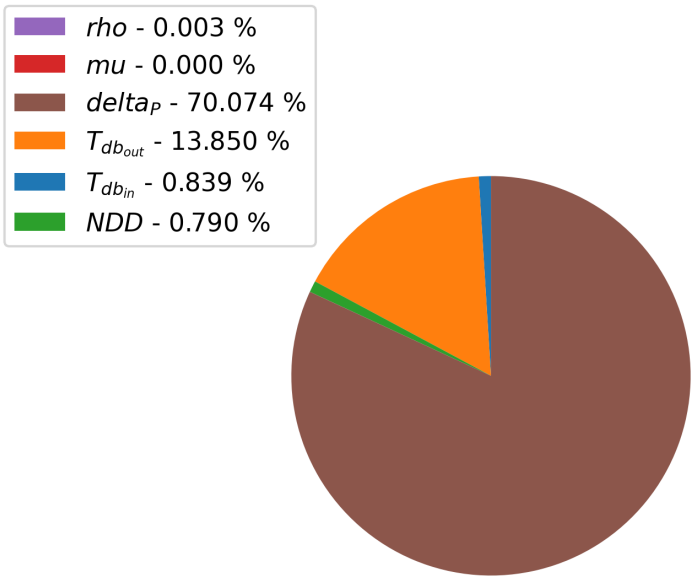

Figure 4.16: Contribution of different variables in calculating air sensible capacity for discharging(heating) test point D1

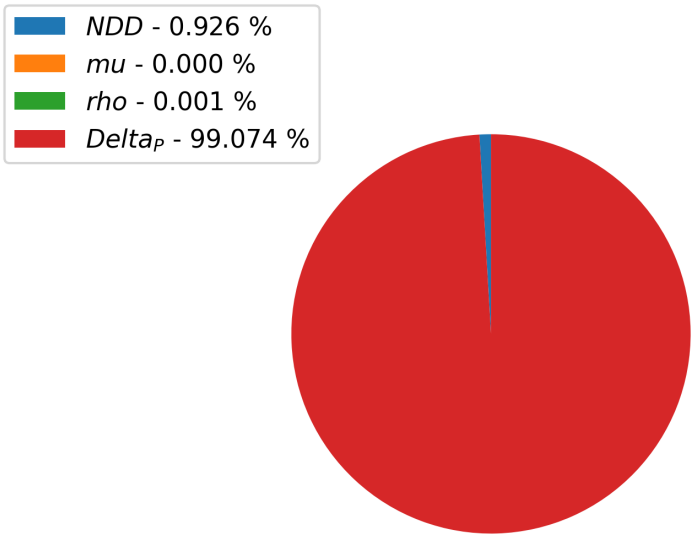

Figure 4.17: Contribution of different variables in calculating air flow rate for discharging(heating) test point D1

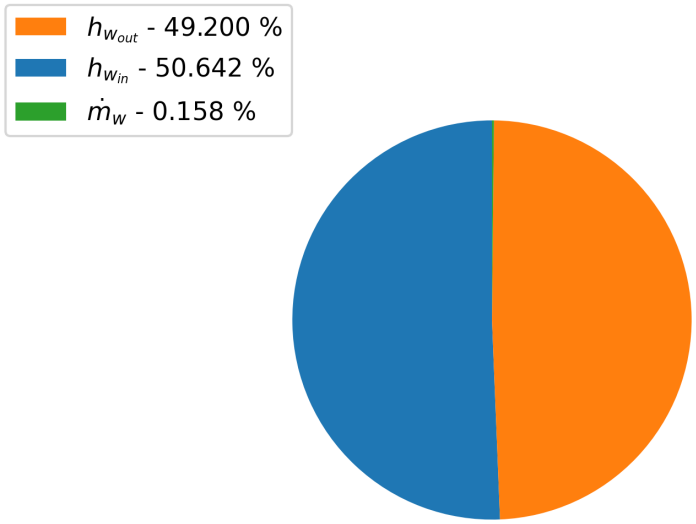

Figure 4.18: Contribution of different variables in calculating water capacity for discharging(heating) test point D1

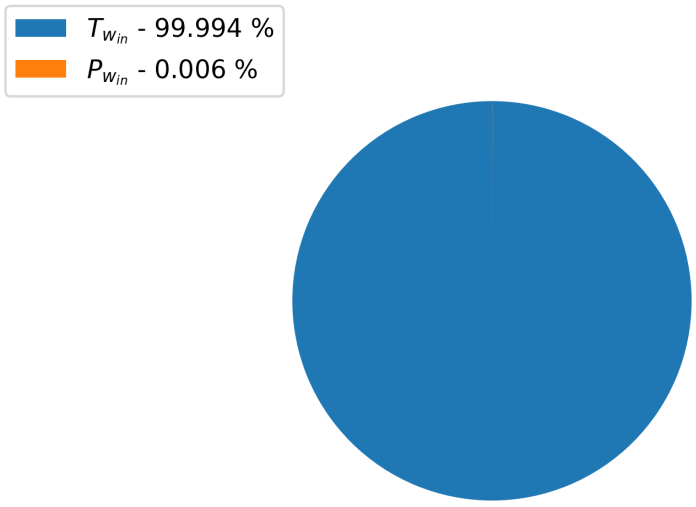

Figure 4.19: Contribution of different variables in calculating water inlet enthalpy for discharging(heating) test point D1

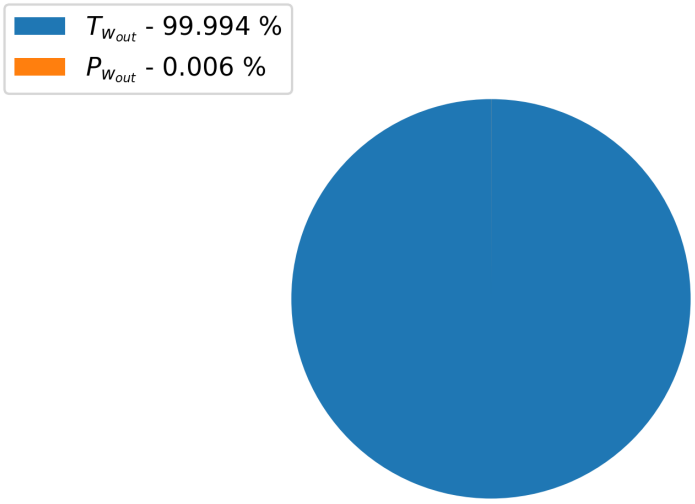

Figure 4.20: Contribution of different variables in calculating water outlet enthalpy for discharging(heating) test point D1

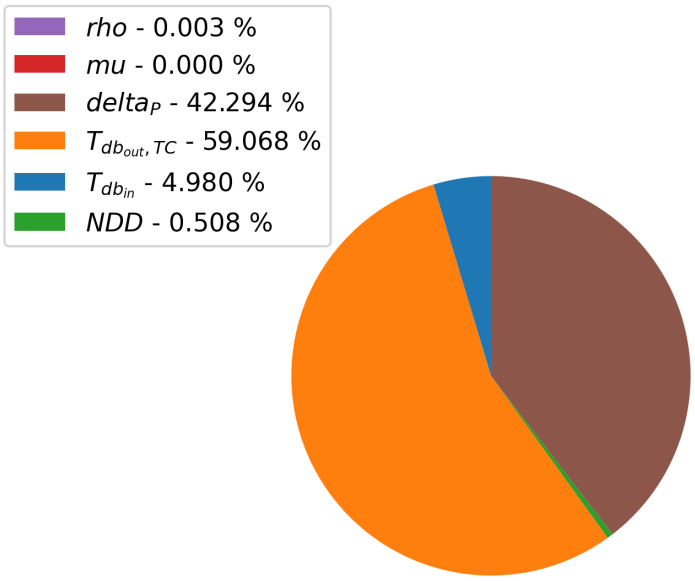

Figure 4.21: Contribution of different variables in calculating air sensible capacity for cooling-charging test point CC7

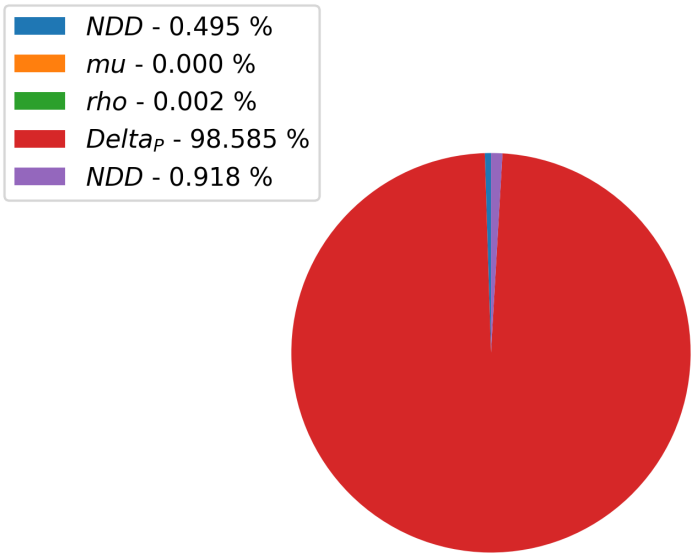

Figure 4.22: Contribution of different variables in calculating air flow rate for cooling-charging test point CC7

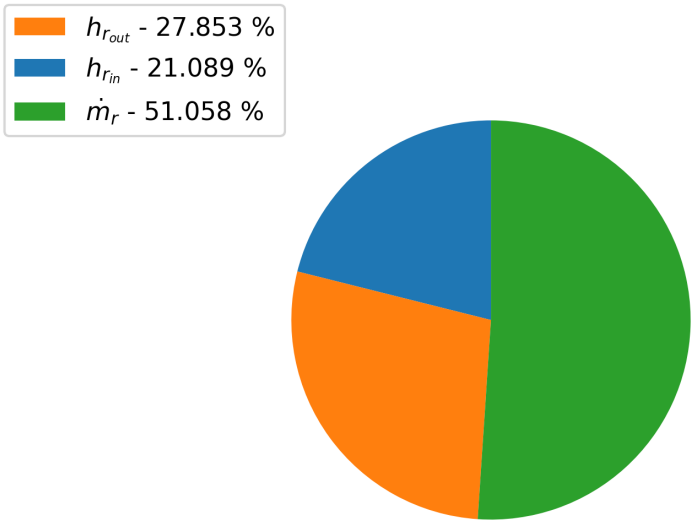

Figure 4.23: Contribution of different variables in calculating refrigerant capacity for cooling-charging test point CC7

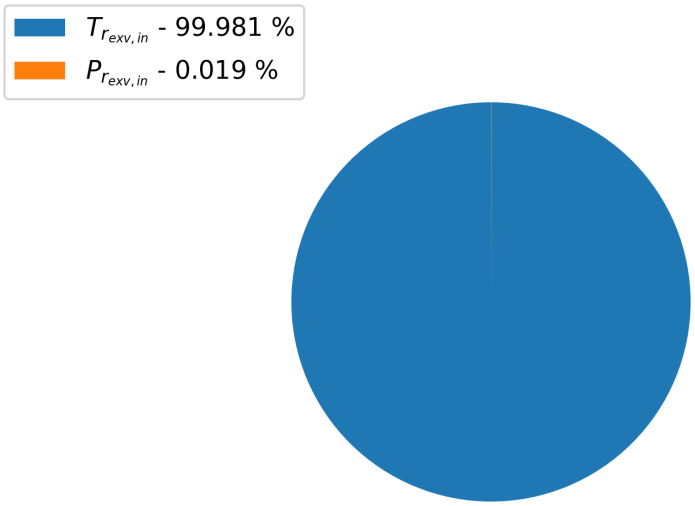

Figure 4.24: Contribution of different variables in calculating refrigerant inlet enthalpy for cooling-charging test point CC7

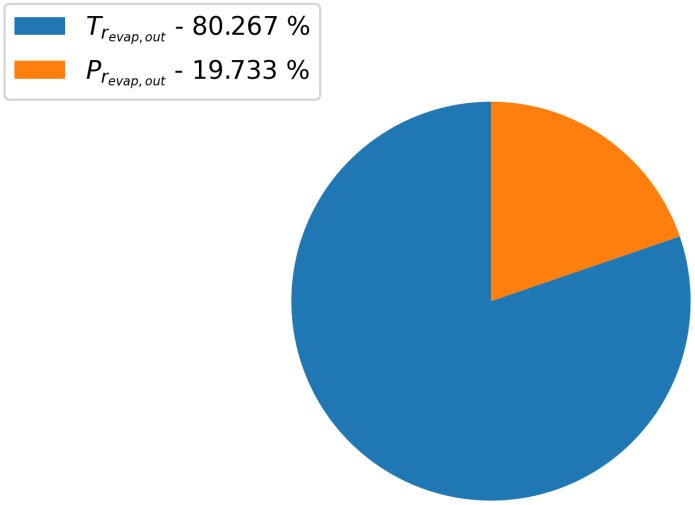

Figure 4.25: Contribution of different variables in calculating refrigerant outlet enthalpy for cooling-charging test point CC7

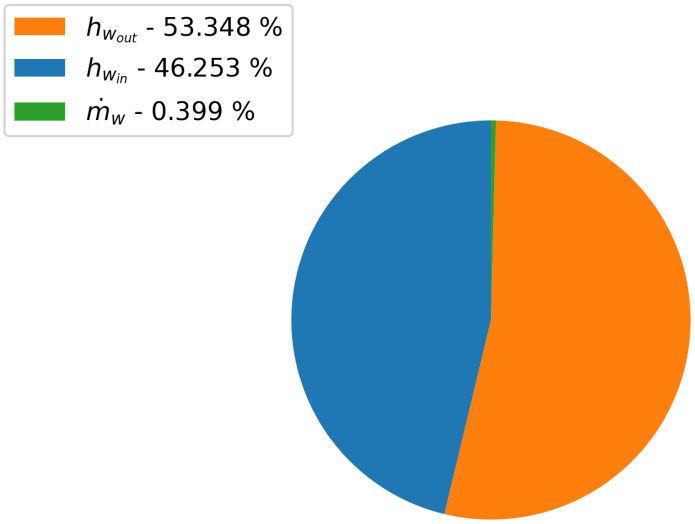

Figure 4.26: Contribution of different variables in calculating water capacity for cooling-charging test point CC7

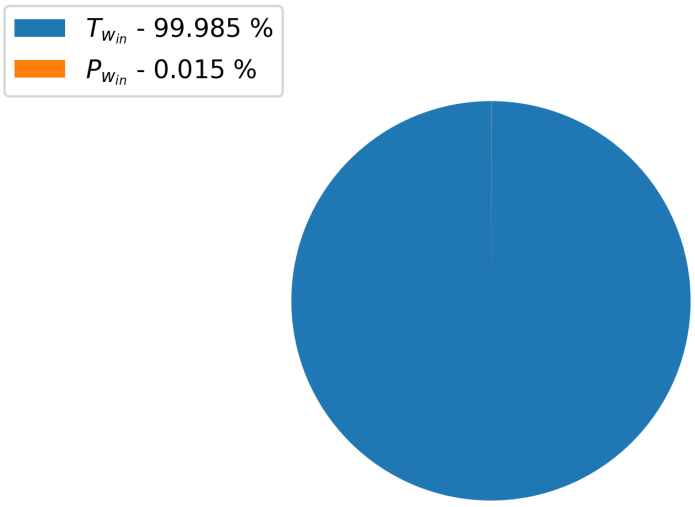

Figure 4.27: Contribution of different variables in calculating water inlet enthalpy for cooling-charging test point CC7

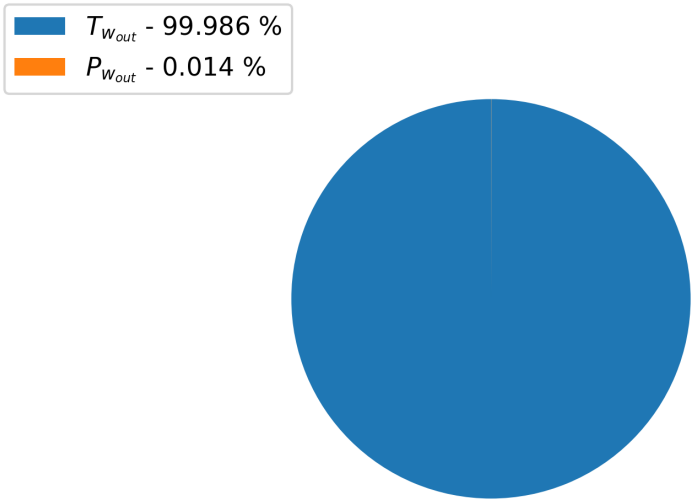

Figure 4.28: Contribution of different variables in calculating water outlet enthalpy for cooling-charging test point CC7

Table 4.14: Uncertainties for TriCoil™ cooling mode air side

Test Point	**Dry Bulb Inlet (±°C)**	**Wet Bulb Inlet (±°C)**	**Dry Bulb Outlet / TC Grid (±°C)**	**ΔP across code tester (±in W.G.)**	**Entering air Pressure (±in W.G.)**	**Air Sensible capacity (±kW)**	**Air sensible capacity uncer. (%)**
C1	0.09	0.13	0.35	0.09	0.27	0.35	4.80
C2	0.09	0.08	0.32	0.09	0.05	0.34	4.43
C3	0.09	0.09	0.32	0.04	0.05	0.48	3.54
C4	0.10	0.09	0.32	0.04	0.05	0.48	3.46

Table 4.15: Uncertainties for TriCoil™ cooling mode refr. side

Test Point	**EXV inlet temp (±°C)**	**EXV inlet pres. Uncer. (±PSIG)**	**Evap outlet temp. (±°C)**	**Evap outlet pres. (±PSIG)**	**Refr. Mass flow rate (±kg/h)**	**Refr. Capacity (±kW)**	**Refr. Capacity Uncer. (%)**
C1	0.35	3.07	2.13	2.35	2.73	0.18	2.33
C2	0.13	0.73	0.18	0.67	0.36	0.02	0.30
C3	0.13	0.75	0.68	0.94	3.22	0.18	1.35
C4	0.13	0.75	0.53	0.84	2.58	0.14	1.05

Table 4.16: Uncertainties for TriCoil™ charging(cooling) mode refr. side

Test Point	**EXV inlet temp (±°C)**	**EXV inlet pres. Uncer. (±PSIG)**	**Evap outlet temp. (±°C)**	**Evap outlet pres. (±PSIG)**	**Refr. Mass flow rate (±kg/h)**	**Refr. Capacity (±kW)**	**Refr. Capacity Uncer. (%)**
CH1	0.13	0.72	0.17	0.68	0.45	0.03	0.24
CH2	0.15	0.89	0.14	0.68	0.52	0.03	0.28
CH3	0.13	0.73	0.13	0.67	0.39	0.03	0.22
CH5	0.16	0.77	0.11	0.69	0.45	0.03	0.31
CH6	0.13	0.73	0.14	0.68	0.38	0.02	0.29
CH7	0.13	0.73	0.12	0.67	0.43	0.03	0.31
CH8	0.15	0.84	0.13	0.69	0.44	0.03	0.34
CH9	0.15	0.81	0.10	0.71	0.57	0.03	0.33
CH10	0.13	0.75	0.15	0.69	0.42	0.03	0.28
CH11	0.13	0.77	0.13	0.68	0.50	0.04	0.23
CH12	0.13	0.75	0.18	0.71	0.44	0.03	0.24
CH13	0.14	0.77	0.20	0.68	0.42	0.03	0.27
CH14	0.13	0.76	0.15	0.67	0.39	0.03	0.25
CH15	0.13	0.75	0.13	0.67	0.43	0.03	0.27

Table 4.17: Uncertainties for TriCoil™ charging(cooling) mode water side

Test Point	**Water Inlet Temp. (±°C)**	**Water Inlet Press. (±PSIG)**	**Water Outlet Temp. (±°C)**	**Press. Diff. across TriCoil (±in W.G.)**	**Water Mass flow rate (±kg/h)**	**Water Capacity (±kW)**	**Water Capacity Uncer.(%)**
CH1	0.09	0.65	0.10	0.38	2.81	0.27	2.01
CH2	0.08	0.65	0.09	0.38	2.78	0.24	2.01
CH3	0.08	0.65	0.09	0.38	1.69	0.15	1.18
CH5	0.08	0.65	0.09	0.38	3.01	0.25	2.78
CH6	0.10	0.66	0.10	0.38	2.92	0.30	3.73
CH7	0.09	0.65	0.09	0.38	1.64	0.15	1.81
CH8	0.09	0.65	0.10	0.38	1.79	0.17	2.16
CH9	0.08	0.65	0.08	0.38	2.74	0.24	2.30
CH10	0.11	0.65	0.11	0.38	1.39	0.19	1.90
CH11	0.08	0.65	0.09	0.38	2.84	0.25	1.66
CH12	0.08	0.65	0.09	0.38	1.69	0.14	1.06
CH13	0.08	0.65	0.09	0.38	2.61	0.25	2.31
CH14	0.08	0.65	0.09	0.38	2.65	0.26	2.50
CH15	0.08	0.65	0.09	0.38	2.60	0.24	2.48

Table 4.18: Uncertainties for TriCoil™ discharging(heating) mode air side

Test Point	**Dry Bulb Inlet (±°C)**	**Wet Bulb Inlet (±°C)**	**Dry Bulb Outlet / TC Grid (±°C)**	**ΔP across code tester (±in W.G.)**	**Entering air Pressure (±in W.G.)**	**Air Sensible capacity (±kW)**	**Air sensible capacity uncer.(%)**
D1	0.08	0.10	0.33	0.09	0.06	0.41	4.52
D2	0.08	0.11	0.32	0.09	0.10	0.34	4.36
D3	0.09	0.09	0.32	0.09	0.06	0.33	4.44
D4	0.09	0.09	0.35	0.09	0.10	0.30	4.85
D5	0.09	0.08	0.32	0.04	0.06	0.44	3.67
D6	0.09	0.08	0.32	0.04	0.07	0.40	3.57
D7	0.09	0.08	0.32	0.04	0.08	0.39	4.32
D8	0.09	0.08	0.32	0.04	0.08	0.40	3.72
D9	0.09	0.08	0.32	0.04	0.05	0.43	3.68
D10	0.12	0.08	0.32	0.04	0.06	0.40	3.94
D11	0.09	0.09	0.32	0.04	0.07	0.38	4.69
D12	0.09	0.08	0.32	0.04	0.05	0.40	4.16

Table 4.19: Uncertainties for TriCoil™ discharging(heating) mode water side

Test Point	**Water Inlet Temp. (±°C)**	**Water Inlet Press. (±PSIG)**	**Water Outlet Temp. (±°C)**	**Press. Diff. across TriCoil (±in W.G.)**	**Water Mass flow rate (±kg/h)**	**Water Capacity (±kW)**	**Water Capacity Uncer.(%)**
D1	0.12	0.66	0.12	0.38	2.89	0.35	4.12
D2	0.10	0.66	0.10	0.38	3.19	0.30	3.96
D3	0.09	0.65	0.09	0.38	3.35	0.26	3.69
D4	0.17	0.66	0.17	0.38	2.83	0.49	8.19
D5	0.08	0.66	0.09	0.38	2.72	0.24	2.13
D6	0.09	0.66	0.09	0.38	2.97	0.26	2.35
D7	0.12	0.65	0.10	0.38	1.08	0.15	1.67
D8	0.10	0.65	0.09	0.38	1.16	0.13	1.23
D9	0.08	0.65	0.09	0.38	2.76	0.24	2.16
D10	0.08	0.65	0.09	0.38	2.80	0.24	2.47
D11	0.09	0.65	0.09	0.38	1.16	0.12	1.57
D12	0.09	0.65	0.08	0.38	1.09	0.12	1.31

Table 4.20: Uncertainties for TriCoil™ cooling-charging mode air side

Test Point	**Dry Bulb Inlet (±°C)**	**Wet Bulb Inlet (±°C)**	**Dry Bulb Outlet / TC Grid (±°C)**	**ΔP across code tester (±in W.G.)**	**Entering air Pressure (±in W.G.)**	**Air Sensible capacity (±kW)**	**Air sensible capacity uncer. (%)**
CC1	0.09	0.08	0.32	0.04	0.06	0.36	5.18
CC2	0.09	0.08	0.32	0.05	0.06	0.35	6.50
CC3	0.09	0.08	0.32	0.04	0.05	0.37	4.35
CC4	0.09	0.08	0.32	0.04	0.06	0.36	4.98
CC5	0.10	0.08	0.32	0.04	0.05	0.36	4.41
CC6	0.09	0.08	0.32	0.04	0.08	0.34	5.13
CC7	0.09	0.08	0.32	0.04	0.06	0.38	4.03
CC8	0.09	0.08	0.32	0.04	0.07	0.37	4.44

Table 4.21: Uncertainties for TriCoil™ cooling-charging mode refr. side

Test Point	**EXV inlet temp (±°C)**	**EXV inlet pres. Uncer. (±PSIG)**	**Evap outlet temp. (±°C)**	**Evap outlet pres. (±PSIG)**	**Refr. Mass flow rate (±kg/h)**	**Refr. Capacity (±kW)**	**Refr. Capacity Uncer. (%)**
CC1	0.18	1.17	0.31	0.69	0.88	0.06	0.40
CC2	0.15	0.84	0.17	0.68	0.60	0.04	0.27
CC3	0.13	0.72	0.14	0.67	0.48	0.03	0.23
CC4	0.13	0.76	0.15	0.67	0.48	0.04	0.23
CC5	0.15	0.91	0.19	0.68	0.58	0.04	0.27
CC6	0.15	0.91	0.15	0.68	0.70	0.05	0.29
CC7	0.14	0.89	0.22	0.69	0.59	0.04	0.29
CC8	0.14	0.80	0.18	0.67	0.52	0.04	0.25

Table 4.22: Uncertainties for TriCoil™ cooling-charging mode water side

Test Point	**Water Inlet Temp. (±°C)**	**Water Inlet Press. (±PSIG)**	**Water Outlet Temp. (±°C)**	**Press. Diff. across TriCoil (±in W.G.)**	**Water Mass flow rate (±kg/h)**	**Water Capacity (±kW)**	**Water Capacity Uncer.(%)**
CC1	0.08	0.65	0.09	0.38	2.86	0.24	3.01
CC2	0.08	0.65	0.08	0.38	2.62	0.24	2.36
CC3	0.09	0.65	0.09	0.38	1.14	0.12	1.97
CC4	0.09	0.65	0.09	0.38	1.12	0.12	1.60
CC5	0.08	0.65	0.09	0.38	3.44	0.25	3.46
CC6	0.08	0.65	0.09	0.38	2.58	0.24	2.63
CC7	0.08	0.65	0.09	0.38	1.13	0.11	2.14
CC8	0.10	0.65	0.09	0.38	1.15	0.13	1.87

4.5 Capacity

To calculate the refrigerant side capacity we have used Equation 4.8

$$\dot{Q}_r = \dot{m}_r(h_{out} - h_{in}) \tag{4.8}$$

Where:

$\dot{Q}_r$ = Heat rejected/gained by refrigerant (W),

$\dot{m}_r$ = mass flow rate of refrigerant (kg/s),

h_{out} = Enthalpy at Tricoil™ outlet (J/kg),

h_{in} = Enthalpy at Tricoil™ inlet (J/kg),

and,

h_{in} = func($T_{exv,in}$, $P_{exv,in}$) and,

h_{out} = func($T_{evap,out}$, $P_{evap,out}$).

Water side capacity has been calculated using equation 4.9

$$\dot{Q}_w = \dot{m}_w C_{p,w}(T_{out} - T_{in}) \tag{4.9}$$

Here,

$\dot{Q}_w$ = Heat rejected/gained by water (W)

$\dot{m}_w$ = mass flow rate of water (kg/s)

$C_{p,w}$ = Specific heat of water (J/kg-K) @ average (T_{out} and T_{in})

T_{out} = Temperature at Tricoil™ outlet (K)

T_{in} = Temperature at Tricoil™ inlet (K)

In this report, we have only run dry coil tests as we were having a heat balance issue with our outlet wet bulb. So the total air capacity would be the sensible capacity of

the air which was determined using Equation 4.10.

$$\dot{Q_{sa}} = \dot{V}_a \rho_a C_{p,a} (T_{db,out} - T_{db,in}) \tag{4.10}$$

Here,

$\dot{Q_{sa}}$ = Sensible Heat rejected/gained by air (W)

$\dot{V}_a$ = volumetric flow rate of air (m^3/s)

$C_{p,a}$ = Specific heat of air (J/kg-K) @ average ($T_{db,out}$ and $T_{db,in}$)

$T_{db,out}$ = Dry bulb temperature at Tricoil™ outlet (K)

$T_{db,in}$ = Dry bulb temperature at Tricoil™ inlet (K)

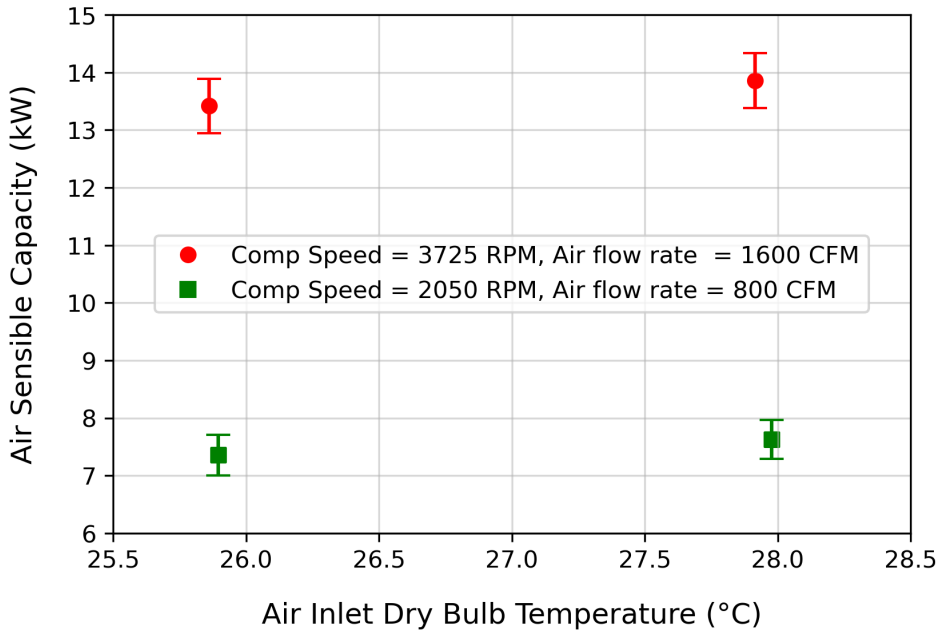

Figure 4.29: Air side sensible capacity of test points at cooling mode

For cooling mode, in Figure 4.29 and Figure 4.30, the capacity increases with compressor speed and inlet air dry bulb temperature.

In charging(cooling) mode for Figure 4.31 and 4.32, the capacity increases with the water inlet temperature and compressor speed. Increasing the mass flow of water also increases the capacity.

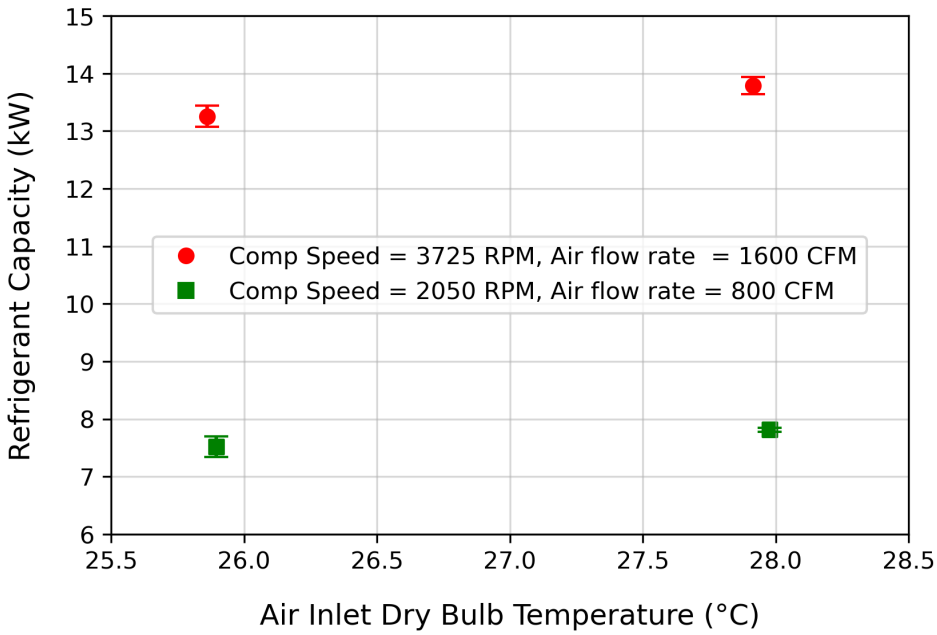

Figure 4.30: Refrigerant side capacity of test points at cooling mode

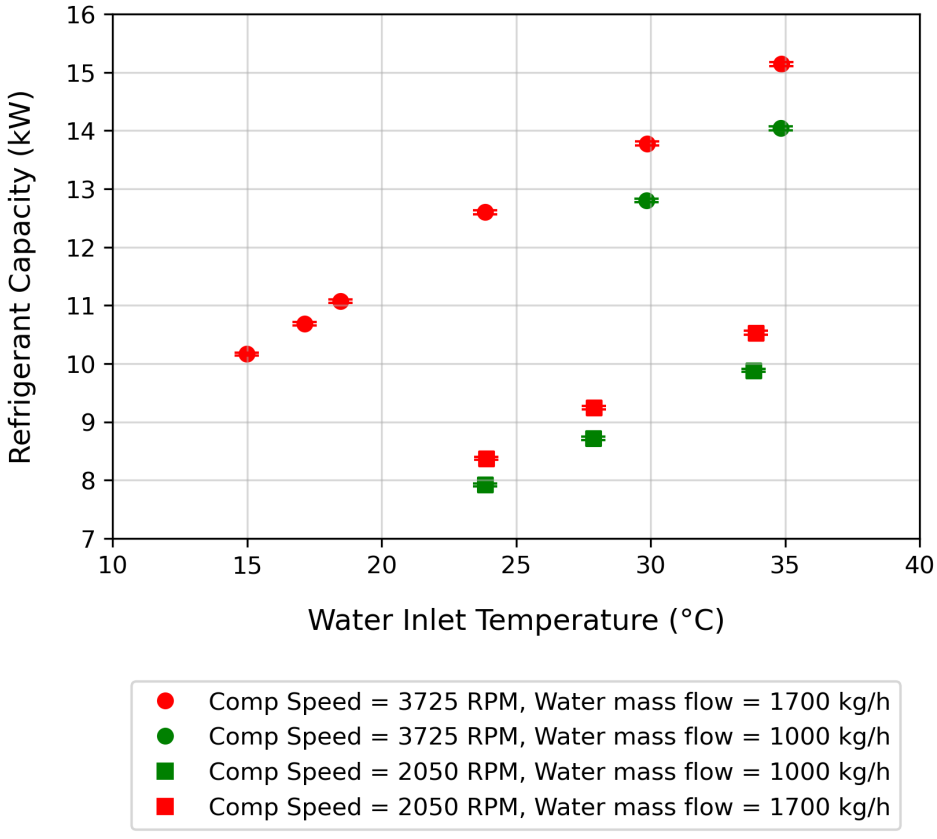

Figure 4.31: Refrigerant side capacity of test points at charging(cooling) mode

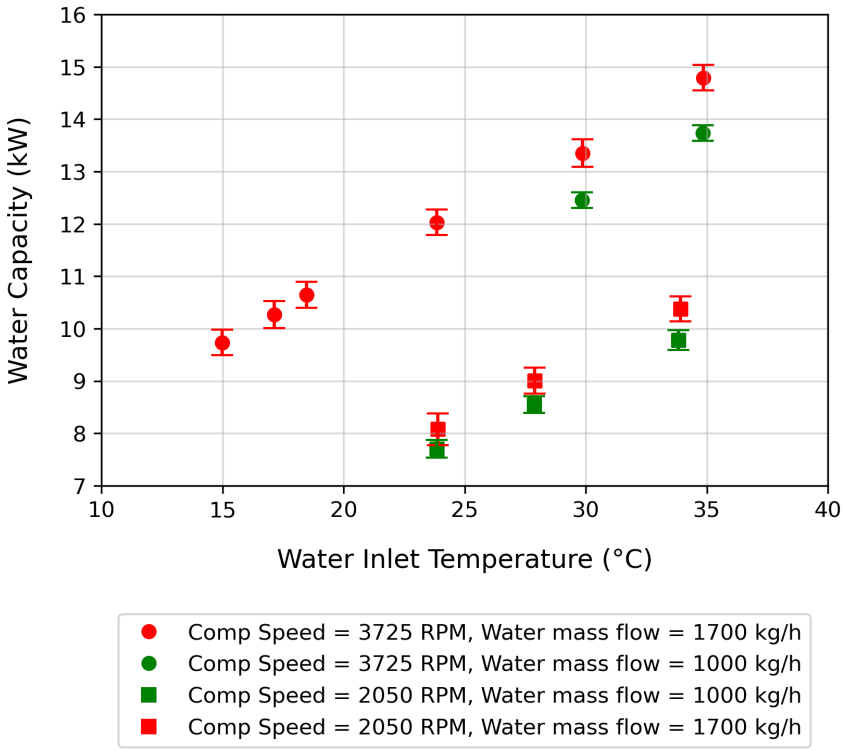

Figure 4.32: Water side capacity of test points at charging(cooling) mode

For the discharging(heating) mode shown in Figure 4.33 and 4.34, capacity increases with air flow rate and decreases with the air inlet dry bulb temperature increasing. The capacity also goes up with inlet water temperature and flow rate.

At Cooling-charging mode in Figure 4.35, 4.36 and 4.37, water side capacity and total capacity go up with the mass flow rate of water, and air side capacity goes down as the water mass flow rate increases. Also, the water capacity increases with decreasing inlet air dry bulb temperature which has an inverse effect on total air side capacity. Total refrigerant side capacity increases with inlet air dry bulb temperature.

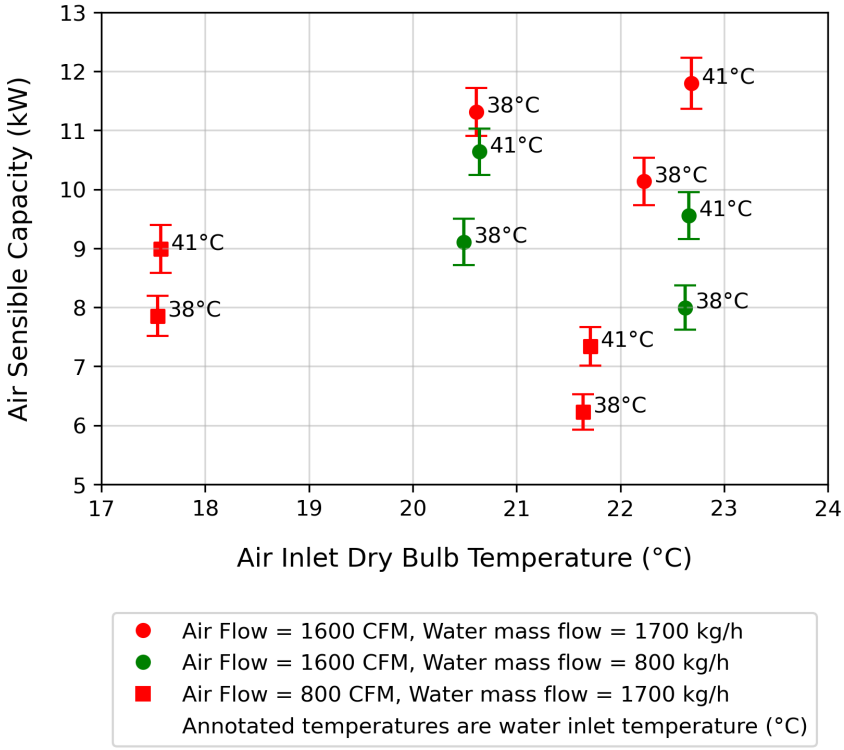

Figure 4.33: Air side sensible capacity of test points at discharging(heating) mode

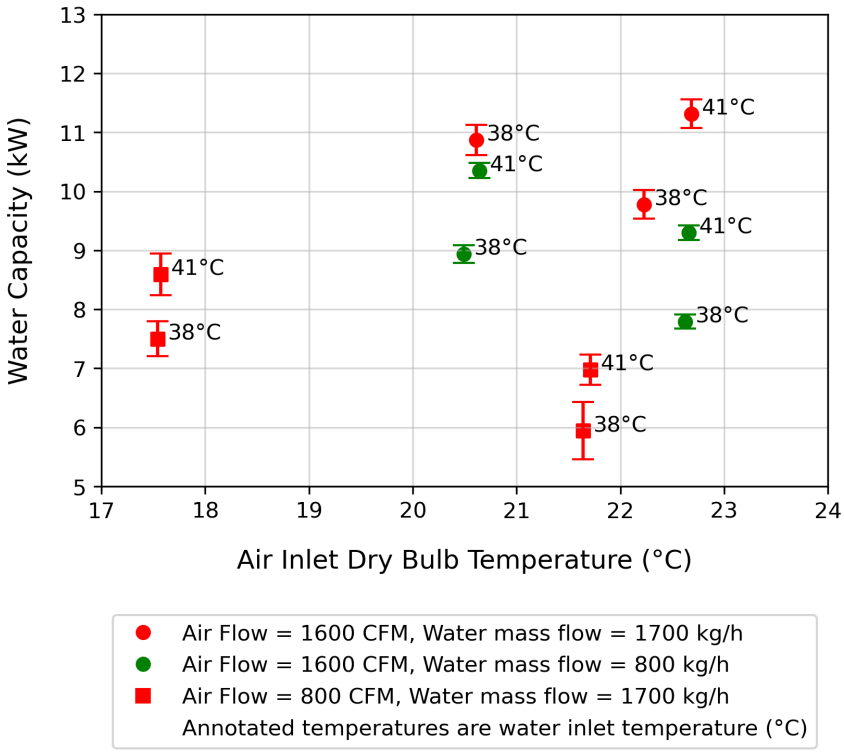

Figure 4.34: Water side capacity of test points at discharging(heating) mode

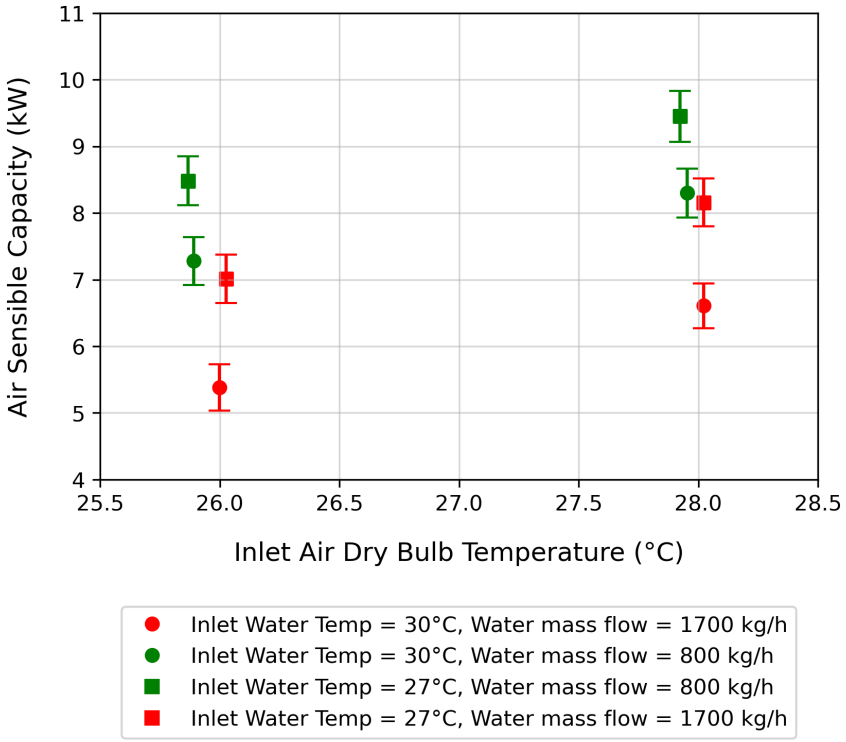

Figure 4.35: Air side capacity of test points at cooling-charging mode

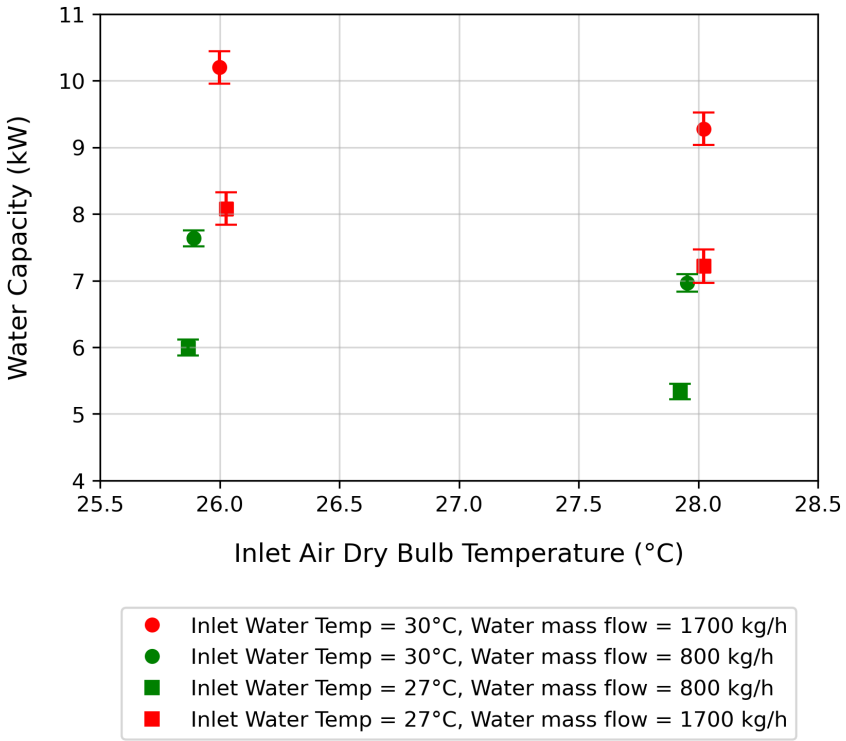

Figure 4.36: Water side capacity of test points at cooling-charging mode

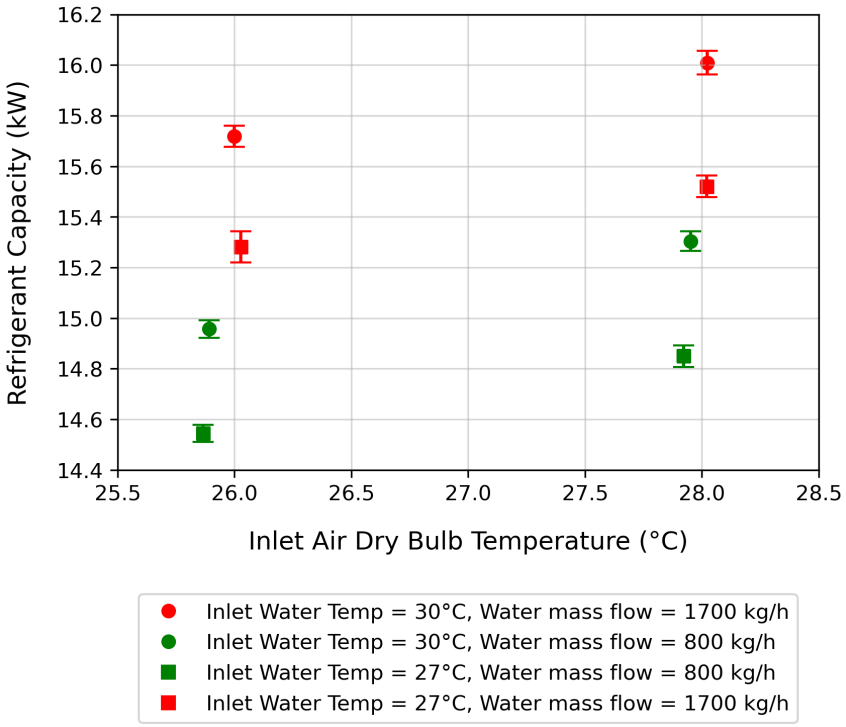

Figure 4.37: Refrigerant side capacity of test points at cooling-charging mode

4.6 UA Values for different modes of TriCoil™

For Cooling, charging (cooling), and discharging (heating) modes, UA (overall heat transfer coefficient) has been calculated [Bowman et al. (1940)]. Equation 4.11 has been used to calculate the LMTD and Equation has been used to calculate UA. Superheat has been neglected on the refrigerant side; superheat values of tests were between 4.5 and 6.5 K.

$$LMTD = \frac{\Delta T_1 - \Delta T_2}{log(\frac{\Delta T_1}{\Delta T_2})} \tag{4.11}$$

$$UA = \frac{Q_{avg}}{LMTD} \tag{4.12}$$

Here,

For Cooling Mode,

$\Delta T_1 = |T_{db,out} - T_{evap,sat}|$

$\Delta T_2 = |T_{db,in} - T_{evap,sat}|$

Q_{avg} = average(Air sensible capacity, Refrigerant capacity)

$T_{db,in}$ = Air inlet dry bulb temperature (°C)

$T_{db,out}$ = Air outlet dry bulb temperature (°C)

$T_{evap,sat}$ = Evaporator Saturation Temperature (°C)

For Charging (cooling) Mode,

$\Delta T_1 = |T_{w,in} - T_{evap,sat}|$

$\Delta T_2 = |T_{w,out} - T_{evap,sat}|$

Q_{avg} = average(Water capacity, Refrigerant capacity)

$T_{w,in}$ = Water inlet temperature (°C)

$T_{w,out}$ = Water outlet temperature (°C)

For discharging (heating) Mode,

$\Delta T_1 = |T_{w,out} - T_{db,in}|$

$\Delta T_2 = |T_{w,in} - T_{db,out}|$

Q_{avg} = average(Water capacity, Air sensible capacity)

Figure 4.38,4.39 and 4.40 shows the UA values of different TriCoil™ modes with the LMTD. Figure 4.41,4.42 and 4.43 shows the capacity of different TriCoil™ modes with the LMTD.

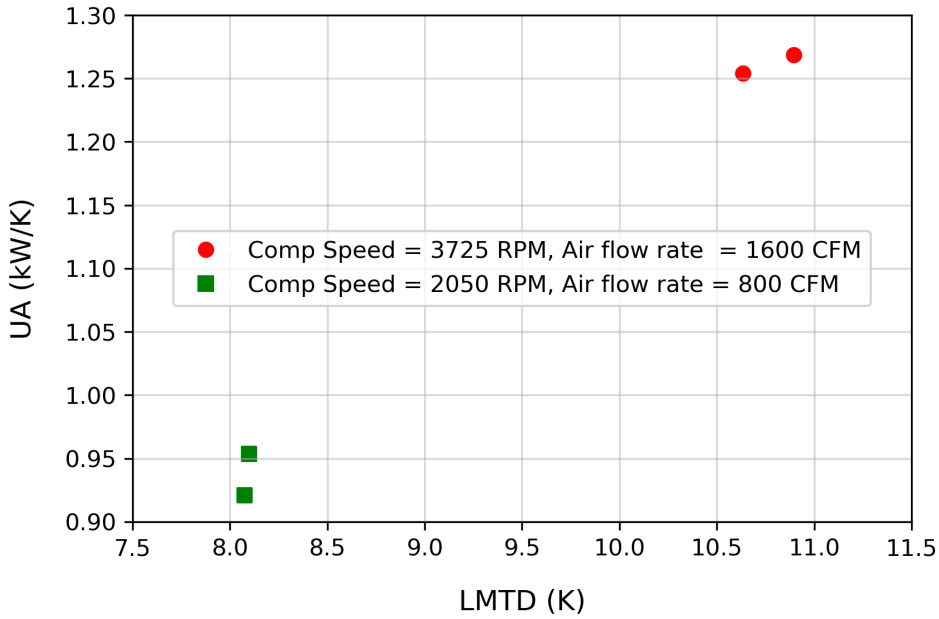

Figure 4.38: UA values for test points at cooling mode

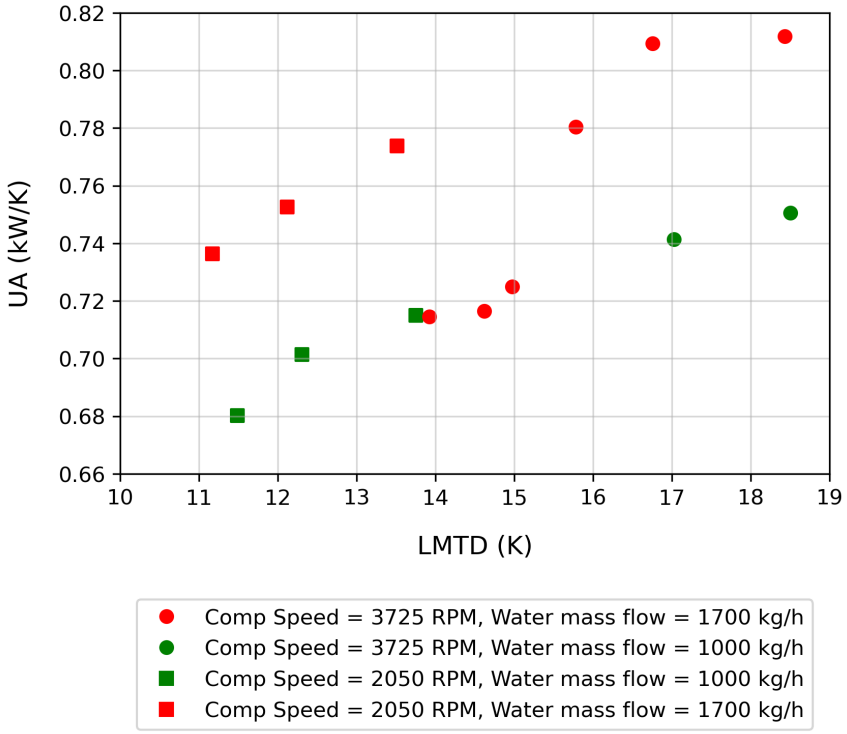

Figure 4.39: UA values for test points at charging (cooling) mode

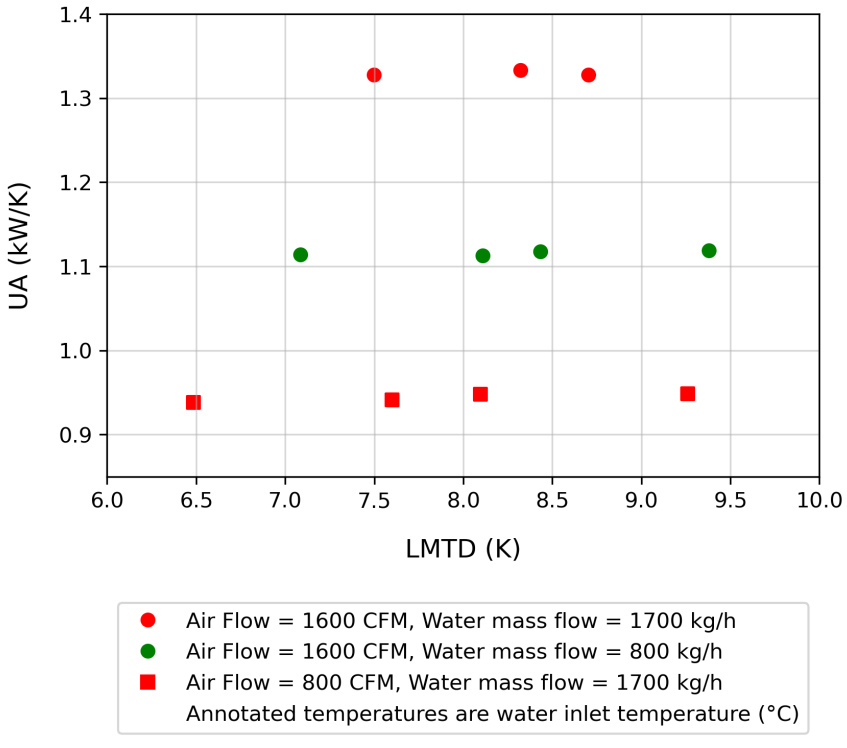

Figure 4.40: UA values for test points at discharging (heating) mode

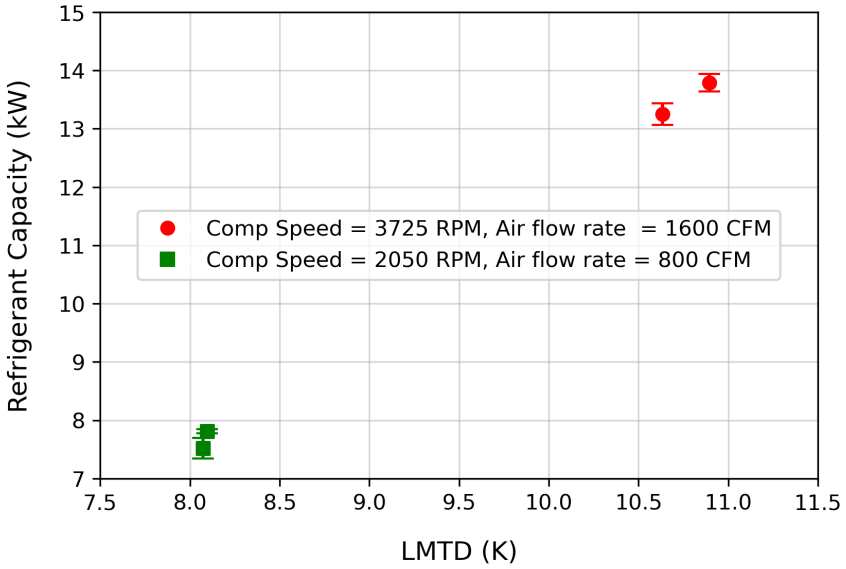

Figure 4.41: Refrigerant side capacity of test points at cooling mode with LMTD

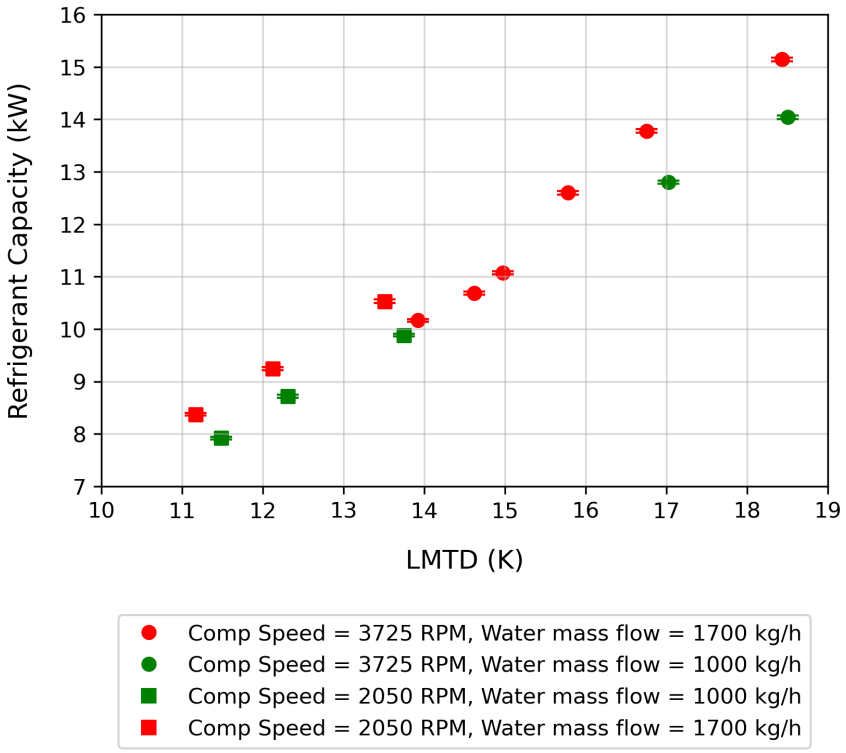

Figure 4.42: Refrigerant side capacity of test points at charging (cooling) mode with LMTD

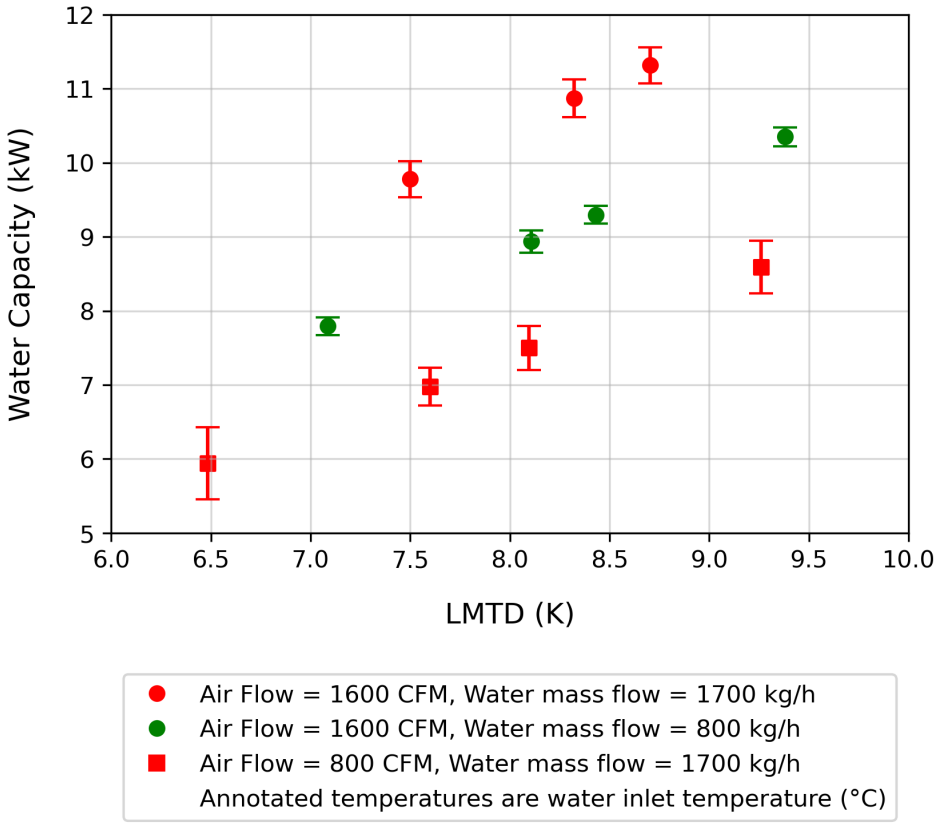

Figure 4.43: Water side capacity of test points at discharging (heating) mode with LMTD

CHAPTER V

CONCLUSION AND FUTURE WORK

5.1 Conclusion

An experimental setup has been developed for a novel three fluid heat exchanger, TriCoil™ inside the wind tunnel at the psychrometric coil facility of OSU. The setup consists of a test duct, a 4-ton heat pump, and a pumped water loop. The TriCoil™ was operated at four different modes- cooling, charging, discharging, and charging-cooling. Different test points were acquired and the heat balance in all modes was found to be between ±5% which validates our test setup according to ASHRAE Standard 33-2016. Uncertainty analysis has also been performed on the test results. On the air side, the pressure difference between the nozzle upstream and downstream is a major source of uncertainty. On the refrigerant side, it was the mass flow rate and the evaporator outlet temperature. On the water side, it was the inlet and outlet temperatures of water. UA values for different modes of TriCoil™ have also been calculated. It is also proved from the experiment done in this thesis that the TriCoil™ can be used effectively to charge TES water. The TES water can also be discharged using TriCoil™.

5.2 Future Work

5.2.1 Acquisition of in-depth test data

A test plan has been developed using the Box-Behnken design from Ferreira et al. (2007) as the current test plan doesn't cover the whole operating range and also

doesn't reflect practical operation scenarios. Test plans for different modes of TriCoil™ are shown from table 5.1 to table 5.6.

Table 5.1: TriCoil™ test plan for charging (cooling) mode

Test Point	Compressor Speed (RPM)	Water Inlet Temp. (°C)	Water mass flow rate (kg/h)
CHC01	2050	10.0	1360
CHC02	3725	10.0	1360
CHC03	2050	25.0	1360
CHC04	3725	25.0	1360
CHC05	2050	17.5	450
CHC06	3725	17.5	450
CHC07	2050	17.5	2270
CHC08	3725	17.5	2270
CHC09	2888	10.0	450
CHC10	2888	25.0	450
CHC11	2888	10.0	2270
CHC12	2888	25.0	2270
CHC13	2888	17.5	1360

Table 5.2: TriCoil™ test plan for charging (heating) mode

Test Point	Compressor Speed (RPM)	Water Inlet Temp. (°C)	Water mass flow rate (kg/h)
CHH01	2050	25.0	1360
CHH02	3725	25.0	1360
CHH03	2050	40.0	1360
CHH04	3725	40.0	1360
CHH05	2050	32.5	450
CHH06	3725	32.5	450
CHH07	2050	32.5	2270
CHH08	3725	32.5	2270
CHH09	2888	25.0	450
CHH10	2888	40.0	450
CHH11	2888	25.0	2270
CHH12	2888	40.0	2270
CHH13	2888	32.5	1360

Table 5.3: TriCoil™ test plan for cooling mode

Test Point	Compressor speed (RPM)	RH% of inlet air	Air inlet temp (°C)	Air flow rate (CFM)
C01	2050	30%	25.0	1200
C02	3725	30%	25.0	1200
C03	2050	80%	25.0	1200
C04	3725	80%	25.0	1200
C05	2050	55%	20.0	1200
C06	3725	55%	20.0	1200
C07	2050	55%	30.0	1200
C08	3725	55%	30.0	1200
C09	2050	55%	25.0	800
C10	3725	55%	25.0	800
C11	2050	55%	25.0	1600
C12	3725	55%	25.0	1600
C13	2888	30%	20.0	1200
C14	2888	80%	20.0	1200
C15	2888	30%	30.0	1200
C16	2888	80%	30.0	1200
C17	2888	30%	25.0	800
C18	2888	80%	25.0	800
C19	2888	30%	25.0	1600
C20	2888	80%	25.0	1600
C21	2888	55%	20.0	800
C22	2888	55%	30.0	800
C23	2888	55%	20.0	1600
C24	2888	55%	30.0	1600

5.2.2 Recommendations for Updating Experimental Setup for Wet Coil Tests

All the tests performed in this test setup so far are dry coil tests. The reason is that we are having a problem with our heat balance using the dry bulb and wet bulb reading from the outlet psychrometer. For this reason, we have relied on the reading of the thermocouple grid average temperature for our outlet dry bulb temperature. One possible reason for this heat balance mismatch might be air leaks into the psychrometer and heat gain of the air inside the psychrometer and connecting ducts.

Table 5.4: TriCoil™ test plan for heating mode

Test Point	Compressor speed (RPM)	Air inlet temp (°C)	Air flow rate (CFM)
H01	2050	15.0	1200
H02	3725	15.0	1200
H03	2050	25.0	1200
H04	3725	25.0	1200
H05	2050	20.0	800
H06	3725	20.0	800
H07	2050	20.0	1600
H08	3725	20.0	1600
H09	2888	15.0	800
H10	2888	25.0	800
H11	2888	15.0	1600
H12	2888	25.0	1600
H13	2888	20.0	1200

Another reason might be as some of the circuits of the TriCoil™ are not active all the time depending on the running mode, there is a large amount of air maldistribution. As air not getting appropriately mixed before the sample tree, we are not getting a proper average reading from the psychrometer. More investigation needs to be done to solve this issue which was not possible due to graduation time constraints.

Another difficulty we faced while running the wet coil test was the steam humidifier of the wind tunnel. The steam humidifier water reservoir is not adequate and it needs frequent refilling when the humidity is low. As the water gets refilled, it causes the whole system to deviate from a steady state. This problem can be solved by installing an auto-leveling valve between the water hose and the reservoir inlet.

5.2.3 Updating Experimental Setup to provide Chilled Water at the TriCoil™ Inlet

There are several other modes of TriCoil™ that we were not able to run, including charging the water while the heat pump is running in heating mode and using cold water from TES to cool down the indoor air. For these modes, we need below ambient

Table 5.5: TriCoil™ test plan for discharging (heating) mode

Test Point	Water inlet temp (°C)	Water mass flow rate (kg/h)	Air inlet temp (°C)	Air flow rate (CFM)
DH01	30.0	450	20.0	1200
DH02	55.0	450	20.0	1200
DH03	30.0	2270	20.0	1200
DH04	55.0	2270	20.0	1200
DH05	30.0	1360	15.0	1200
DH06	55.0	1360	15.0	1200
DH07	30.0	1360	25.0	1200
DH08	55.0	1360	25.0	1200
DH09	30.0	1360	20.0	800
DH10	55.0	1360	20.0	800
DH11	30.0	1360	20.0	1600
DH12	55.0	1360	20.0	1600
DH13	42.5	450	15.0	1200
DH14	42.5	2270	15.0	1200
DH15	42.5	450	25.0	1200
DH16	42.5	2270	25.0	1200
DH17	42.5	450	20.0	800
DH18	42.5	2270	20.0	800
DH19	42.5	450	20.0	1600
DH20	42.5	2270	20.0	1600
DH21	42.5	1360	15.0	800
DH22	42.5	1360	25.0	800
DH23	42.5	1360	15.0	1600
DH24	42.5	1360	25.0	1600

water temperature at the TriCoil™ inlet and that can be achieved using the chiller developed by Makhani (2020). Unfortunately, the chiller has not been commissioned yet. To complete the commissioning process, the VFD of the compressor of the chiller needs to be set up and the refrigerant loop developed by Chowdhury (2021) needs to be leak tested and charged. Alternatively, we can also use the lab chilled water supply to get inlet water temperature below 6°C.

5.2.4 Developing a Gray Box Model

A gray box model can be developed from the test result to predict the capacity of the TriCoil™ indoor coil and outlet fluid properties. A correction factor for LMTD can be tuned by the experimental data available for the gray box model.

Table 5.6: TriCoil™ test plan for discharging (cooling) mode

Test Point	Water inlet temp (°C)	Water mass flow rate (kg/h)	RH% of inlet air	Air inlet temp (°C)	Air flow rate (CFM)
DC01	5.0	450	55%	25.0	1200
DC02	20.0	450	55%	25.0	1200
DC03	5.0	2270	55%	25.0	1200
DC04	20.0	2270	55%	25.0	1200
DC05	5.0	1360	30%	25.0	1200
DC06	20.0	1360	30%	25.0	1200
DC07	5.0	1360	80%	25.0	1200
DC08	20.0	1360	80%	25.0	1200
DC09	5.0	1360	55%	20.0	1200
DC10	5.0	1360	55%	30.0	1200
DC11	20.0	1360	55%	30.0	1200
DC12	5.0	1360	55%	25.0	800
DC13	20.0	1360	55%	25.0	800
DC14	5.0	1360	55%	25.0	1600
DC15	20.0	1360	55%	25.0	1600
DC16	12.5	450	30%	25.0	1200
DC17	12.5	2270	30%	25.0	1200
DC18	12.5	450	80%	25.0	1200
DC19	12.5	2270	80%	25.0	1200
DC20	12.5	450	55%	20.0	1200
DC21	12.5	2270	55%	20.0	1200
DC22	12.5	450	55%	30.0	1200
DC23	12.5	2270	55%	30.0	1200
DC24	12.5	450	55%	25.0	800
DC25	12.5	2270	55%	25.0	800
DC26	12.5	450	55%	25.0	1600
DC27	12.5	2270	55%	25.0	1600
DC28	12.5	1360	30%	20.0	1200
DC29	12.5	1360	80%	20.0	1200
DC30	12.5	1360	30%	30.0	1200
DC31	12.5	1360	80%	30.0	1200
DC32	12.5	1360	30%	25.0	800
DC33	12.5	1360	80%	25.0	800
DC34	12.5	1360	30%	25.0	1600
DC35	12.5	1360	80%	25.0	1600
DC36	12.5	1360	55%	20.0	800
DC37	12.5	1360	55%	30.0	800
DC38	12.5	1360	55%	20.0	1600
DC39	12.5	1360	55%	30.0	1600
DC40	12.5	1360	55%	25.0	1200

REFERENCES

Al-Shannaq, R., Kurdi, J., Al-Muhtaseb, S., Dickinson, M., and Farid, M. (2015). Supercooling elimination of phase change materials (pcms) microcapsules. *Energy*, 87:654–662.

Albanakis, C., Yakinthos, K., Kritikos, K., Missirlis, D., Goulas, A., and Storm, P. (2009). The effect of heat transfer on the pressure drop through a heat exchanger for aero engine applications. *Applied Thermal Engineering*, 29(4):634–644.

Alghamdi, K. I. (2022). Water-based thermal energy storage for heating and air-conditioning applications in residential buildings: Review and preliminary study.

Alva, G., Lin, Y., and Fang, G. (2018). An overview of thermal energy storage systems. *Energy*, 144:341–378.

Arteconi, A., Hewitt, N. J., and Polonara, F. (2012). State of the art of thermal storage for demand-side management. *Applied Energy*, 93:371–389.

ASHRAE (1987). Ashrae standard 41.2-1987, standard methods for laboratory airflow measurement. ashrae inc. atlanta, ga.

ASHRAE (2016). Ashrae standard 33-2016, method of testing forced circulation air cooling and air heating coils. ashrae inc. atlanta, ga.

ASHRAE (2018). Ashrae standard 41.2-2018, standard methods for air velocity and airflow measurement. ashrae inc. atlanta, ga.

ASME (2013). Asme ptc 19.1-2013 test uncertainty (revision of asme ptc 19.1-2005.

Bach, C. K. and Spitler, J. D. (2021). Ar21-037, research plan submitted to ocast for novel water-refrigerant-air heat exchanger, tricoil.

Bach, C. K. L. (2014). *Refrigerant side compensation for air-side maldistribution of evaporators and its effects on system performance*. Ph.d.

Bell, I. H. and Groll, E. A. (2011). Air-side particulate fouling of microchannel heat exchangers: Experimental comparison of air-side pressure drop and heat transfer with plate-fin heat exchanger. *Applied Thermal Engineering*, 31(5):742–749.

Bowman, R., Mueller, A., and Nagle, W. (1940). Mean temperature difference in design. *Transactions of the American Society of Mechanical Engineers*, 62(4):283–293.

Chowdhury, I. (2021). Design and construction of a pumped refrigerant loop for commercial scale low-gwp refrigerant heat exchanger testing.

Cirocco, L., Pudney, P., Riahi, S., Liddle, R., Semsarilar, H., Hudson, J., and Bruno, F. (2022). Thermal energy storage for industrial thermal loads and electricity demand side management. *Energy Conversion and Management*, 270.

Coils, D. and University, P. (2014). Dbm coils technologies. https://dbmcoils.com/wind-tunnel/.

Cristofari, C., Notton, G., Poggi, P., and Louche, A. (2003). Influence of the flow rate and the tank stratification degree on the performances of a solar flat-plate collector. *International Journal of Thermal Sciences*, 42(5):455–469.

De Schampheleire, S., De Jaeger, P., Huisseune, H., Ameel, B., T'Joen, C., De Kerpel, K., and De Paepe, M. (2013). Thermal hydraulic performance of 10 ppi aluminium foam as alternative for louvered fins in an hvac heat exchanger. *Applied Thermal Engineering*, 51(1-2):371–382.

EIA (2018). 2018 commercial buildings energy consumption survey. https://www.eia.gov/consumption/commercial/data/2018/pdf/cbecs%202018%20ce%20release%202%20flipbook.pdf.

EIA (2022). Table 2.1a energy consumption: Residential, commercial, and industrial sectors. https://www.eia.gov/totalenergy/data/monthly/pdf/sec2$_4$.*pdf*.

Emerson (2021). Product data sheet for micro motion™ elite™ coriolis flow and density meters. https://www.emerson.com/documents/automation/product-data-sheet-micro-motion-elite-coriolis-flow-density-meters-en-66748.pdf.

Ferreira, S. L., Bruns, R. E., Ferreira, H. S., Matos, G. D., David, J. M., Brandao, G. C., da Silva, E. G., Portugal, L. A., dos Reis, P. S., Souza, A. S., and dos Santos, W. N. (2007). Box-behnken design: an alternative for the optimization of analytical methods. *Anal Chim Acta*, 597(2):179–86. Ferreira, S L C Bruns, R E Ferreira, H S Matos, G D David, J M Brandao, G C da Silva, E G P Portugal, L A dos Reis, P S Souza, A S dos Santos, W N L eng Netherlands 2007/08/09 Anal Chim Acta. 2007 Aug 6;597(2):179-86. doi: 10.1016/j.aca.2007.07.011. Epub 2007 Jul 23.

Gan, G. and Riffat, S. B. (1997). Pressure loss characteristics of orifice and perforated plates. *Experimental thermal and fluid science*, 14(2):160–165.

Garg, H. P., Mullick, S., and Bhargava, V. K. (2012). *Solar thermal energy storage*. Springer Science Business Media.

Gil, A., Medrano, M., Martorell, I., Lázaro, A., Dolado, P., Zalba, B., and Cabeza, L. F. (2010). State of the art on high temperature thermal energy storage for power generation. part 1—concepts, materials and modellization. *Renewable and Sustainable Energy Reviews*, 14(1):31–55.

Green, J. H., Rogers, R. D., Sapper, J. P., Brandel, P. E., and Wilson, D. S. (1982). Three media heat exchanger capable of heat exchange.

Hasnain, S. (1998a). Review on sustainable thermal energy storage technologies, part i: heat storage materials and techniques. *Energy conversion and management*, 39(11):1127–1138.

Hasnain, S. (1998b). Review on sustainable thermal energy storage technologies, part ii: cool thermal storage. *Energy conversion and management*, 39(11):1139–1153.

Heng, K. L. (2017). Modeling and control strategy of geothermal heat pump water chiller-heater with dual thermal storage water tanks.

Hollands, K. and Lightstone, M. (1989). A review of low-flow, stratified-tank solar water heating systems. *Solar energy*, 43(2):97–105.

Huang, Z., Ling, J., Bacellar, D., Hwang, Y., Aute, V., and Radermacher, R. (2020). Airside thermal and hydraulic characteristics of compact bare tube heat exchanger under dry and wet conditions. *International Journal of Refrigeration*, 110:295–307.

Huisseune, H., T'Joen, C., De Jaeger, P., Ameel, B., De Schampheleire, S., and De Paepe, M. (2013). Performance analysis of a compound heat exchanger by screening its design parameters. *Applied Thermal Engineering*, 51(1-2):490–501.

Johnson-Controls (2019). Hx(tm)3 touch screen thermostat - models: S1-thxu430w.

Kim, G. T., Choi, Y. U., Chung, Y., Kim, M. S., Park, K. W., and Kim, M. S. (2018). Experimental study on the performance of multi-split heat pump system with thermal energy storage. *International Journal of Refrigeration*, 88:523–537.

Kincheloe, M. C., Franke, J. P., Bach, C. K., and Bradshaw, C. R. (2021). Design of a psychrometric coil testing facility for commercial size heat exchanger coils. *International Journal of Refrigeration*, 121:143–151.

Le, K. X., Huang, M. J., Shah, N., Wilson, C., Mac Artain, P., Byrne, R., and Hewitt, N. J. (2019). High temperature air source heat pump coupled with thermal energy

storage: Comparative performances and retrofit analysis. *Energy Procedia*, 158:3878–3885.

Lee, J. and Domanski, P. A. (1997). Impact of air and refrigerant maldistributions on the performance of finned-tube evaporators with r-22 and r-407c.

Lee, M., Kim, Y., Lee, H., and Kim, Y. (2010). Air-side heat transfer characteristics of flat plate finned-tube heat exchangers with large fin pitches under frosting conditions. *International Journal of Heat and Mass Transfer*, 53(13-14):2655–2661.

Liang, C., Wang, Y., and Li, X. (2022). Energy-efficient air conditioning system using a three-fluid heat exchanger for simultaneous temperature and humidity control. *Energy Conversion and Management*, 270.

Liu, X., Shi, L., Qu, M., and Warner, J. (2019). A preliminary study of a novel heat pump integrated underground thermal energy storage for shaping electric demand of buildings. Report, Oak Ridge National Lab.(ORNL), Oak Ridge, TN (United States).

Makhani, K. K. (2020). Design, simulation, and construction of a hot-gas bypass chiller for a commercial scale psychrometric coil testing facility.

Marković, S., Jaćimović, B., Genić, S., Mihailović, M., Milovančević, U., and Otović, M. (2019). Air side pressure drop in plate finned tube heat exchangers. *International Journal of Refrigeration*, 99:24–29.

Mokarram, N. H. and Wang, H. (2022). Design and modeling of novel two-phase heat exchangers for a home cooling system with ice energy storage. *Applied Thermal Engineering*, 207.

Novoselac, A. and Bourne, S. (2021). Us patent no: Us 11,041,680 b2; high-density latent heat storage device.

Romero-Méndez, R., Sen, M., Yang, K., and McClain, R. L. (1997). Effect of tube-to-tube conduction on plate-fin and tube heat exchanger performance. *International journal of heat and mass transfer*, 40(16):3909–3916.

Saffari, M., de Gracia, A., Fernández, C., Belusko, M., Boer, D., and Cabeza, L. F. (2018). Optimized demand side management (dsm) of peak electricity demand by coupling low temperature thermal energy storage (tes) and solar pv. *Applied Energy*, 211:604–616.

Saleem, S., Sarfraz, O., Bradshaw, C. R., and Bach, C. K. (2020). Development of novel experimental infrastructure for collection of high-fidelity experimental data for refrigerant to air heat exchangers. *International Journal of Refrigeration*, 114:189–200.

Sarfraz, O., Bach, C. K., and Bradshaw, C. R. (2019). Discrete modeling of fin-and-tube heat exchangers with cross-fin conduction functionality. *International Journal of Refrigeration*, 104:270–281.

Sarfraz, O., Bach, C. K., and Bradshaw, C. R. (2020). Validation of advanced fin-and-tube heat exchanger models with cross-fin conduction functionality. *International Journal of Refrigeration*, 116:70–81.

Sebzali, M. J., Ameer, B., and Hussain, H. J. (2014). Comparison of energy performance and economics of chilled water thermal storage and conventional air-conditioning systems. *Energy and Buildings*, 69:237–250.

SPP (2022). Southwest power pool forecast vs. actual for 2022-09-20, website: https://marketplace.spp.org/pages/forecast-vs-actual.

Wen, M.-Y. and Ho, C.-Y. (2009). Heat-transfer enhancement in fin-and-tube heat exchanger with improved fin design. *Applied Thermal Engineering*, 29(5-6):1050–1057.

York (2017). Technical guide - affinity(tm) series split system heat pumps - models: Yzv24 thru 60.

York (2019). Technical guide - single piece variable speed ecm communicating air handlers with electronic expansion valve, models: Avv series.

Zhang, H., Shao, S., Xu, H., Zou, H., Tang, M., and Tian, C. (2016). Numerical investigation on fin-tube three-fluid heat exchanger for hybrid source hvacr systems. *Applied Thermal Engineering*, 95:157–164.

Zhou, D., Zhao, C. Y., and Tian, Y. (2012). Review on thermal energy storage with phase change materials (pcms) in building applications. *Applied Energy*, 92:593–605.

VITA

Farhan Istiaque

Candidate for the Degree of

Master of Science

Thesis: DEVELOPMENT AND COMMISSIONING OF A VARIABLE CAPACITY EXPERIMENTAL INFRASTRUCTURE FOR A NOVEL THREE FLUID HEAT EXCHANGER

Major Field: Mechanical and Aerospace Engineering

Biographical:

Education:

Completed the requirements for the degree of Master of Science with a major in Mechanical and Aerospace Engineering at Oklahoma State University in May 2023.

Received a Bachelor of Science in Mechanical Engineering at Bangladesh University of Engineering and Technology in February 2017.